Lawrence Berkeley National Laboratory

Title
Optical Transient-Grating Measurements of Spin Diffusion and Relaxation in a Two-Dimensional Electron Gas

Permalink
https://escholarship.org/uc/item/15t9d238

Author
Weber, Christopher P.

Publication Date
2005-12-15

Optical Transient-Grating Measurements of Spin Diffusion and Relaxation in a Two-Dimensional Electron Gas

by

Christopher Phillip Weber

B.A. (University of California, Berkeley) 1999
M.S. (University of California, Berkeley) 2003

A dissertation submitted in partial satisfaction
of the requirements for the degree of

Doctor of Philosophy

in

Physics

in the

GRADUATE DIVISION

of the

UNIVERSITY OF CALIFORNIA, BERKELEY

Committee in charge:

Professor Joseph Orenstein, Chair
Professor Mike Crommie
Professor Eugene Haller

Fall 2005

Optical Transient-Grating Measurements of Spin Diffusion and Relaxation in a
Two-Dimensional Electron Gas

Abstract

Optical Transient-Grating Measurements of Spin Diffusion and Relaxation in a
Two-Dimensional Electron Gas

by

Christopher Phillip Weber

Doctor of Philosophy in Physics

University of California, Berkeley

Professor Joseph Orenstein, Chair

Spin diffusion in n-GaAs quantum wells, as measured by our optical transient-grating technique, is strongly suppressed relative to that of charge. Over a broad range of temperatures and dopings, the suppression of D_s relative to D_c agrees quantitatively with the prediction of "spin Coulomb drag" theory, which takes into account the exchange of spin in electron-electron collisions.

Moreover, the spin-diffusion length, L_s, is a nearly constant 1 μm over the same range of T and n, despite D_s's varying by nearly two orders of magnitude. This constancy supports the D'yakonov-Perel'-Kachorovskii model of spin relaxation through interrupted precessional dephasing in the spin-orbit field.

Professor Joseph Orenstein
Dissertation Committee Chair

1

Contents

Acknowledgement

Chapter 1

Introduction

1.1 Spin transport and diffusion

An electron propagating through a solid carries spin angular momentum in addition to its mass and charge. Of late there has been considerable interest in developing electronic devices based on the transport of spin[1], in hope that they might offer advantages in dissipation, size, and speed over charge-based devices[2]. It has been suggested, however, that spin-based field-effect transistors are likely to have higher power consumption and longer switching times than their charge-based counterparts[3], and are additionally unlikely to do anything that a charge-based transistor does not[4].

Whatever the prospects of spin-based devices, the introduction of spin into electronics brings with it additional complexity. The electrical current carried by a gas of electrons is simply proportional to its total momentum, so the charge current is not affected by (non-Umklapp) electron-electron (e-e) collisions[5]. However, since the electron's spin along a given spatial direction can take the values $\pm\hbar/2$ (conventionally $\uparrow, \downarrow$), the spin current need not be proportional to the momentum. Although the transport of spin polarization is not protected by momentum conservation, it has been widely assumed that, like the charge current, spin current is unaffected by e-e interactions. The primary result of this work is to demonstrate experimentally not only that this assumption is invalid, but that over a broad range of temperature and electron density, the flow of spin polarization in a two-dimensional gas of electrons is controlled by the rate of e-e collisions[6].

The experiments that I report here were conducted to investigate propagation and dephasing of spin populations, characterized by the spin-diffusion coefficient D_s and the spin decay rate τ_s^{-1}. The Einstein relation, a special case of the fluctuation-dissipation theorem, relates D_s to its

accompanying conductivity, σ_s, and many-body susceptibility, $\chi_s \equiv \partial s / \partial B$:

$$D_s = \frac{\sigma_s}{e^2 \chi_s}. \tag{1.1}$$

Spin diffusion thus measures spin transport. The effect of e-e collisions on spin transport is to suppress D_s relative to the charge-diffusion coefficient—in these measurements, by as much as a factor of 7.5. I find this suppression to agree quantitatively with the "spin Coulomb drag" theory of D'Amico and Vignale[7,8].

Spin polarization in GaAs quantum wells is believed to relax primarily through the D'yakonov-Perel'-Kachorovskii mechanism of precessional dephasing in the spin-orbit field. In this case, D_s has a further significance, through the prediction that $D_s \tau_s = const$, explained in Chapter 4. Si *et al.*[9] have suggested further that the spin-charge separation postulated to occur in correlated-electron materials ought to show up as a difference between the diffusion coefficients of spin and charge.

1.2 The transient spin grating

In this work, I characterize spin diffusion in a two-dimensional electron gas (2DEG) by the transient-spin-grating technique[10], which is based on optical injection of spin-polarized electrons. The 2DEG resides in a GaAs quantum well; near-bandgap illumination of the GaAs excites electrons whose initial spin is determined by the helicity of the light[11]. If the GaAs is excited by two non-collinear, coherent beams of light with orthogonal linear polarization, then in the region where the beams interfere the helicity varies sinusoidally from plus to minus one. The optical-helicity wave generates a wave of electron-spin polarization with the same spatial frequency, which in turn generates a sinusoidal variation (the eponymous "grating") in the index of refraction through the Kerr effect.

The time-evolution of the transient spin grating directly reveals the nature of spin transport and relaxation in the electronic system, functioning like a time-domain version of neutron scattering. I measure the spin polarization by detecting the diffraction of a probe beam off the grating. A sensitive coherent detection scheme enables acquisition of the ~ 150 grating decays required to characterize the spin dynamics of each 2DEG throughout a broad temperature-wavevector parameter space.

1.3 Prior measurements of D_s

Other than this work, to my knowledge only three measurements of spin diffusion in GaAs have been published; two used the transient-spin-grating method. Allan Miller's group[10] measured

an undoped GaAs/AlGaAs quantum well of width 6.5 nm. They estimated the background concentration as p-type, with $n = 6.5 \times 10^9$ cm^{-2}. Measuring at room temperature, they found that $D_s = 127$ cm^2/s and $\tau_s = 55$ ps. In a conference proceeding[12], Keith Nelson's group reported measurement of an undoped quantum well of width 6.8 nm, but did not say at what temperature. They found $D_s = 58$ cm^2/s and $\tau_s = 17$ ps.

David Awschalom's group[13] measured n-type, bulk GaAs with $n = 10^{16}$ cm^{-3}, at 1.6 K. Their experiment involved photo-injecting a population of spin-polarized electrons, which drifted in an applied electric field, and were detected at distances up to 100 μm away. They didn't explicitly state D_s, but if one naïvely takes calipers to their graph, one gets $D_s = 100$ cm^2/s and $\tau_s = 28,000$ ps. This estimate, however, fails to take into account the Coulomb interaction between electrons and holes, which tends to "stretch" the spin-packet, making D_s appear to be larger than it is[14].

Chapter 2

Transient Spin Gratings

2.1 Probing spin dynamics with transient gratings

Transient grating spectroscopy (TGS) is an experimental tool that is capable of selectively inducing and probing fluctuations of charge and spin density. It is a two-step, or pump-probe, technique in which a spatially varying modulation of spin or charge is first introduced by the interference of two "pump" laser pulses. In the second step, the time-evolution of the modulation is measured by the diffraction of a "probe" beam. Measuring the time-dependence of the modulation as a function of its wavevector gives direct information about the collective and single-particle excitations that govern spin or charge transport. The combination of pump-probe spectroscopy and sensitivity to spin and charge provides an additional degree of freedom—one can introduce a density fluctuation and probe the resulting spin fluctuation (or vice versa). The transient spin grating, used in these experiments, was first introduced by Cameron *et al.*[10].

2.1.1 Optical orientation in GaAs

The transient spin grating is based on the optical orientation of electron spins: near-bandgap illumination of a GaAs quantum well excites electrons whose initial spin is determined by the helicity of the light[11].

The valence and conduction bands of GaAs derive from p- and s-orbitals, and so have $j = \frac{3}{2}$ and $j = \frac{1}{2}$, respectively, near the zone center. Confinement in a quantum well splits the valence band's $m_j = \pm\frac{3}{2}$ (heavy hole) and $m_j = \pm\frac{1}{2}$ (light hole), with the heavy hole at higher energy. The situation is shown schematically in Fig. 2.1.1. Conservation of angular momentum requires that,

(j, mj)

CB   (1/2, 1/2)   (1/2, -1/2)

σ_- $\sigma+$

HH   (3/2, 3/2) σ_- $\sigma+$ (3/2, -3/2)

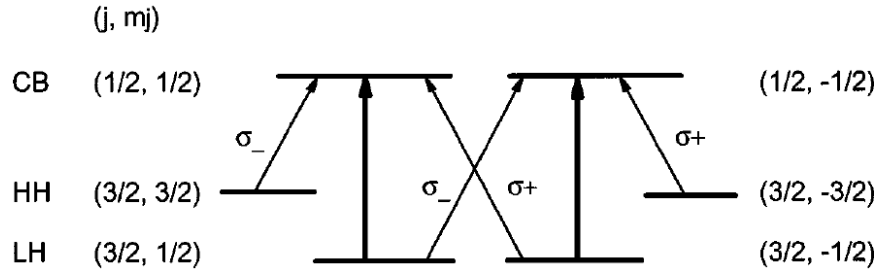LH   (3/2, 1/2)   (3/2, -1/2)

Figure 2.1. A representation of the selection rules for optical transitions between the valence and conduction bands of a GaAs quantum well. The figure is taken from Cameron *et al.*[10]. Here m_j is taken along the direction of the incident light. $\sigma_\pm$ labels allowed transitions due to the absorption of right- and left-circularly polarized light.

for absorption of right-circularly-polarized light, only those transitions with $\Delta m_j = +1$ (labeled σ_+) are allowed; illumination with left circular allows only σ_- transitions.

One can photoexcite GaAs with light that has sufficient energy to excite electrons from the heavy-hole band, but not from the light-hole band. Then if the light is, for instance, right-circularly polarized, it will induce transitions only from $\left(\frac{3}{2}, -\frac{3}{2}\right)$ to $\left(\frac{1}{2}, -\frac{1}{2}\right)$, resulting in a completely spin-polarized population of electrons and holes. (Even in the bulk material, in which the heavy- and light-hole bands are degenerate at the zone center, partial spin orientation is possible. The probabilities of transitions from the $m_j = \pm\frac{3}{2}$ and $m_j = \pm\frac{1}{2}$ states are in a 3:1 ratio[15].)

Immediately after photoexcitation, the electron and hole spins lie along the direction of illumination—that is, in the growth direction of the quantum well. The direction of the hole spin rapidly randomizes due to scattering. Because the conduction band derives from an atomic s-orbital, electrons lose spin memory much more slowly than the holes. Therefore, for time delays longer than ~ 1 picosecond, the spin memory resides exclusively in the nonequilibrium electron population.

2.1.2   Generating the transient grating

A transient grating is generated by a pair of coherent pulses traveling with a relative angle θ. Their interference produces a standing wave in the plane of the sample, with an electric field,

$$\vec{E} \propto \hat{e}_1 e^{i\phi(x)} + \hat{e}_2 e^{-i\phi(x)}, \tag{2.1}$$

where $\hat{e}_1$ and $\hat{e}_2$ are the polarization vectors for the two pulses, $\phi(x) = kx\sin\theta$, and k is the wavevector of the incident light. The time-averaged intensity in the plane has a spatially varying component proportional to $\hat{e}_1 \cdot \hat{e}_2$. The intensity contrast is a maximum when $\hat{e}_1$ and $\hat{e}_2$ are parallel, while for $\hat{e}_1 \perp \hat{e}_2$ the intensity is spatially uniform. Nevertheless, orthogonal pulses do create a standing wave, but of photon helicity rather than intensity. If, for example, the beams are
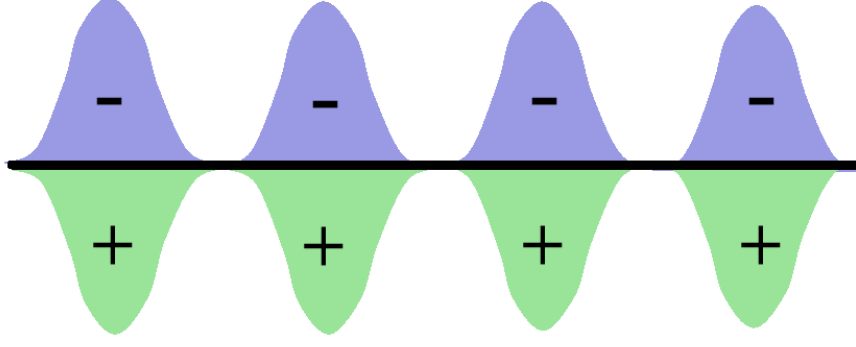
Figure 2.2. A representation of the charge grating produced by interference of two beams with parallel linear polarizations. Because the Coulomb interaction between electrons and holes enforces local charge neutrality, the grating diffuses at the slower rate of the holes.
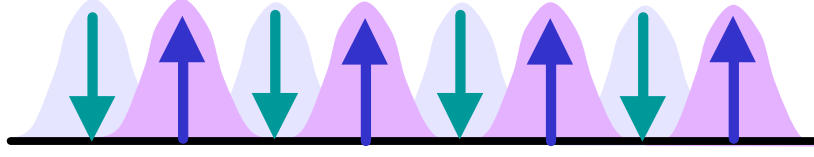

Figure 2.3. A representation of the spin grating produced by interference of two beams with perpendicular linear polarizations. The electron and hole populations do not vary spatially.

polarized along x and y, we can express the total electric field in the circularly-polarized basis:

$$\vec{E} \propto \hat{e}_+ \cos(\phi + \pi/2) + \hat{e}_- \sin(\phi + \pi/2), \tag{2.2}$$

where $\hat{e}_\pm = \hat{x} \pm i\hat{y}$. The intensity of the electromagnetic field at the surface is

$$I = I_+ \cos^2(\phi + \pi/2) + I_- \sin^2(\phi + \pi/2), \tag{2.3}$$

where $I_\pm$ is the intensity in the positive (negative) sense of helicity. The intensity at the sample surface can be viewed as the sum of standing waves of left and right circularly polarized intensity that are shifted relative to each other by a quarter wavelength.

Generation of an intensity or helicity wave creates two distinct patterns of excitation in the semiconductor as illustrated in Figs. 2.2 and 2.3. The intensity standing wave generates a sinusoidal modulation of nonequilibrium electron-hole density (Fig. 2.2), while the electron-hole density is uniform for the helicity wave (Fig. 2.3). However, photon helicity couples directly to the spin of the carriers because of spin-orbit splitting of the valence band.

2.1.3 Probing the transient grating

After the coherent pulse pair generates nonequilibrium states with spatial modulation of carrier and spin density, the coupled spin and charge dynamics of the semiconductor are encoded in the subsequent time-evolution of the modulation. The information can be decoded because the nonequilibrium carriers perturb the index of refraction, n, of the semiconductor medium, creating a transient diffraction grating. The carrier density modulation creates an index change δn that is independent of polarization. By contrast, a modulation of spin density generates circular optical birefringence—that is, an index difference for left- and right-circularly polarized light.

The evolution through time of the nonequilibrium state can be measured by diffracting a probe beam from the transient grating. Both types of gratings are probed most effectively with linearly polarized light. A beam diffracted from a carrier-density grating emerges with its polarization unchanged, while the polarization of a probe diffracted from a spin grating is rotated by 90 degrees. (This difference is extremely helpful in distinguishing the two gratings experimentally.)

The origin of the polarization rotation from the spin grating can be seen by viewing the linear polarization state of the probe as a superposition of left and right circular states. After diffracting from the grating, the relative phase of the left and right components of the probe are phase shifted by 90 degrees, reflecting the quarter-wave spatial shift between the spin-up and spin-down electron populations. The 90-degree phase shift between left and right circular components corresponds to a 90-degree rotation when reexpressed in the linear polarization basis.

2.1.4 Key innovations

Despite the technique's elegance and potential power, only a handful of spin-grating decay curves appear in the literature (to myknowledge only Cameron *et al.*[10] and Adachi *et al.*[12]), reflecting the previous difficulties inherent in the measurement. The diffracted signal has typically been weak, slowing acquisition of data and making it difficult to reject stray light. The ability, in principle, to scan wavevector by changing the relative angle of the two pump beams has been difficult to implement in practice: each new wavevector required almost a complete optical realignment, involving changing the direction of the pump beams and repositioning of the detection optics.

Our implementation of the transient grating technique[16] solves these problems, thereby creating new opportunities for experiments not feasible with conventional techniques. (The work presented in Section 3.2 alone required acquisition of ~ 450 grating decays.) Here I discuss two features that are key to our experiment: (1) replacing the conventional beamsplitter with a phase-mask array; and (2) introducing phase-modulated heterodyne detection of the diffracted wave.

In our transient grating apparatus, as in a standard pump-probe experiment, the laser beam is first divided into pump and probe beams by using a conventional beamplitter. An optical delay line introduces a variable delay into the probe beam's path. In the next stage, both beams are focused

onto a transmission grating fabricated using silica phase-mask technology. (The phase masks are described more fully in Appendix A.) The phase mask is designed to maximize the energy diffracted into the ± 1 orders. Four beams, two for pumping and two for probing, emerge from the phase mask, and are focused onto the sample surface using a spherical mirror. The pump beams generate a transient grating whose wavelength is one-half of the wavelength of the transmission grating from which they are derived. Because the two probes emerge from the same transmission grating as the pumps, a phase-matching condition is automatically satisfied—the component of each probe diffracted from the transient grating is scattered exactly into the beam path of the transmitted component of the other.

Creating pulse pairs with a phase mask solves the two most serious problems inherent in the conventional implementation of the transient grating experiment. First, we are able to scan the transient grating wavevector without any need for optical realignment. To accomplish this we use a phase mask array consisting of ten transmission gratings, with different wavelengths, etched onto the same silica wafer. The wavelength of the transient grating is changed simply by translating the array so that a different transmission grating is placed at the appropriate focus. In the detection stage another spherical mirror and phase mask array convert the ± 1 orders back into a zeroth-order beam. Thus the detector and associated focusing and filtering optics remain fixed as well during the wavevector scan. Second, the signal-to-noise and stray light rejection is tremendously enhanced by a phase-modulated coherent detection scheme. As mentioned above, a diffracted probe emerges from the sample colinearly with the transmitted part of the other probe. These two pulses coherently mix at a photodiode detector to produce a photocurrent signal,

$$i \propto E_{trans} \cdot E_{diff} \cos\theta, \qquad (2.4)$$

where E_{trans} and E_{diff} are the electric fields of the transmitted and diffracted probe, respectively, and θ is their relative phase. In this scheme the signal is proportional to the amplitude rather than intensity of the diffracted wave[17,18,16]. Considering that E_{diff}/E_{trans} is typically of order $10^{-5} - 10^{-4}$, coherent detection enhances the ratio of signal to stray light by four or five orders of magnitude. Furthermore, the sensitivity of the signal to the phase angle θ allows for a large improvement in signal-noise ratio. In our apparatus a thin wafer of glass is mounted on a torsional oscillator and placed in the path of one of the probe beams. Oscillating the angle of the glass causes θ to vary sinusoidally, selectively modulating the component of the photocurrent signal that comes from the diffracted wave. We measure the photocurrent with a lock-in amplifier synchronized to the torsional oscillator's frequency. This reduces the effect of the 1/f fluctuations of the probe beam's amplitude, which are the dominant source of noise in the experiment.

2.2   Details of our measurement

For the measurements reported here, the wavevector of the injected spin-density wave is in the plane of the 2DEG and the spin polarization is oriented perpendicular to this plane. The two interfering beams that generate the optical-helicity wave derive from a Ti:Sapphire laser, which produces a train of optical pulses with duration 100 fs, interpulse separation 11 ns and center wavelength 820 nm. The incident power density for most measurements was ~ 500 W/cm^2, corresponding to ~ 6 W/cm^2 absorbed per quantum well (or 3×10^{11} cm^{-2} photoexcited electrons per well per laser pulse). For $T > 35$ K grating decay rates did not change when measured at incident powers down to 100 W/cm^2, suggesting that photoinduced holes do not play a significant role in the electron spin transport (typical electron-hole recombination times were ~ 750 ps). At low T the grating decay rate increased slowly with decreasing power, consistent with an electron heating model described in Section 3.2.3.

The grating wavevector was directed along the GaAs $(01\bar{1})$ direction. The torsional oscillator modulates the relative phase of the two beams sinusoidally at frequencies between 210 Hz and 1.2 kHz. Synchronous detection with a lock-in amplifier at the modulation frequency leads to considerable rejection of laser noise and stray light.

Chapter 3

Spin Diffusion in 2-D: Observation of Spin Coulomb Drag

3.1 About our samples

The main results of this work derive from measurements on three samples: $GaAs/Ga_{0.7}Al_{0.3}As$ quantum wells, grown in the (100) direction by molecular beam epitaxy by Jason Stephens of David Awschalom's group. Each consisted of ten quantum wells of thickness 12 nm, separated by 48 nm barriers. The Si impurities were deposited in eight single atomic layers in the center 14 nm of each barrier to maximize their distance from the 2DEG. The carrier concentration, n, mobility, μ, and electrical resisitivity ρ were measured using 4-probe transport techniques without illumination. For the samples with n of 7.8, 4.3, and 1.9 $\times 10^{11}$ cm^{-2} per quantum well, at low temperature μ reached 240,000, 92,000, and 69,000 cm^2/V-s, respectively. The improved screening of the dopant-ion potential at higher n most likely accounts for the increased mobility.

A later generation of samples consisted of 30 quantum wells each; the magnitude of the pump-probe modulation signal was correspondingly bigger than in the ten-well samples. In another set of samples we deliberately introduced disorder by depositing a portion of the Si dopants in the well, randomly distributed. A few results from the sample with 83% of the dopant in the well appear below.

For a system with 12 nm wells and $Ga_{1-x}Al_xAs$ barriers where $x =$0.3, the bottom of the second subband is 70 meV above the bottom of the first subband.[19] This energy is significantly larger than the Fermi energies of the three samples, which are 8.7, 19, and 34 meV. Thus at low temperatures there are essentially no carriers in the second subband. Figure 3.1 shows the expected fraction
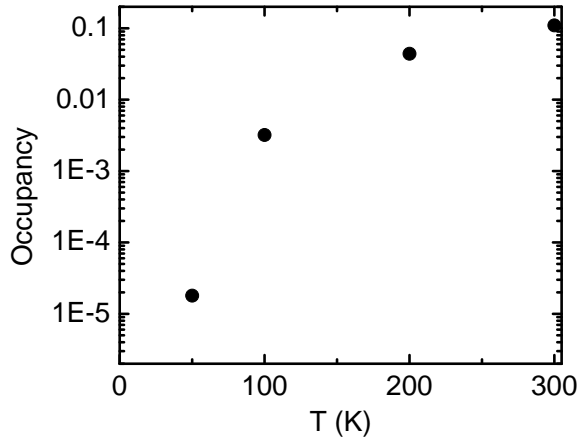
Figure 3.1. Occupancy of the 2nd subband of the sample with $T_F = 400$ K, as a function of temperature.

of carriers in the second subband as a function of T for the sample with the highest density (the fraction is entirely negligible for the two lower-density samples).

At room temperature the occupancy is estimated to be 11% and it decreases rapidly with decreasing T. As will be described below, the ratio of spin and charge transport coefficients is observed to agree with the theory of spin Coulomb drag over the entire range from 40 K, where occupancy of the second subband is negligible, up to room temperature. In view of this agreement, and the agreement observed in the lower electron density samples where the fractional occupation of the second subband is small at all temperatures, we don't believe that the second subband affects the comparison of theory and experiment.

3.2 Measurement of non-disordered, (100) quantum wells

Our main results are for three quantum well samples, with electron concentrations of 7.8, 4.3, and 1.9 $\times 10^{11}$ cm^{-2}, corresponding to Fermi temperatures of 400, 220, and 100 K, and to Fermi velocities v_F of 3.7, 2.7, and 1.8 $\times 10^7$ cm/s, respectively. Fig. 3.2 shows the initial decay rate of the spin grating as a function of T in the most heavily doped sample, for several grating wavevectors from 0.4×10^4 cm^{-1} to 2.5×10^4 cm^{-1}. The dependence on T can be described in terms of three regions. For 100 K $< T <$ 300 K the decay rate varies slowly. For 50 K $< T <$ 100 K the decay rate increases rapidly with decreasing T, and for $T < 50$ K it reaches a slowly varying plateau.

We begin by discussing the decay rate where it varies slowly, *i.e.*, below 50 K and above 100 K. In the high-T region the spin dynamics can be accurately described in terms of independent processes of spin diffusion and spin relaxation. In this description, the decay rate varies with q quadratically, as $\gamma_q = \tau_s^{-1} + D_s q^2$, where D_s is the spin diffusion coefficient and τ_s is the spin
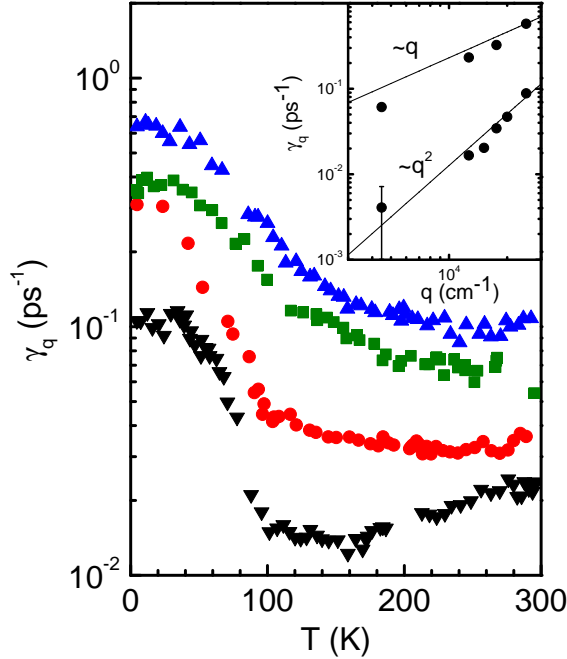
Figure 3.2. Spin-grating decay at various q, T for the sample with $T_F = 400$ K. **Main panel:** The initial decay rate, γ_q, of the spin grating as a function of T for (bottom to top) $q = 0.45$, 1.3, 1.8, 2.5 $\times 10^4$ cm^{-1}. **Inset:** The initial decay rate of the spin grating as a function of q. Points are $\gamma_q - \tau_s^{-1}$; τ_s is obtained from decay of homogenous ($q = 0$) spin excitation. Error bars are the size of the points except as shown. **Lower points and line:** Room temperature. The line is a fit of the data to $\gamma_q = \tau_s^{-1} + D_s q^2$. **Upper points and line:** 5K. The line has slope=1, corresponding to ballistic, rather than diffusive, spin-motion with a velocity of 2.3×10^7 cm/s.

relaxation time[10]. In the inset to Fig. 3.2 we plot $\gamma_q - \tau_s^{-1}$ *vs.* q at 295 K (lower points) and 5 K (upper points), on logarithmic axes. Here $1/\tau_s$ is independently determined from the decay rate of the circular dichroism induced by a circularly polarized pump beam[20] (see Chapter 4). A comparison of the 295 K data with a line of slope two shows that the decay of the grating is well described by diffusive dynamics: a fit of the data to $\gamma_q = \tau_s^{-1} + D_s q^2$ gives $D_s = 130$ cm^2/s and $\tau_s = 50$ ps, yielding a spin diffusion length $L_s = (D_s \tau_s)^{1/2} = 0.81$ μm and a "spin mean-free-path" $l = 2D_s/v_F = 60$ nm. The observation of diffusive motion is internally consistent, as l is much smaller than both L_s and the smallest grating wavelength, 2.5 μm.

3.2.1 Model for ballistic-diffusive crossover

Next, we examine the spin-grating dynamics at $T < 50$ K. As shown in the inset, the initial decay rates at 5 K are linear in q at the higher wavevectors. The change in power law exponent

from two to one indicates that a crossover from diffusive to ballistic dynamics takes place as the sample temperature is lowered. In the ballistic regime electrons propagate a distance comparable to the grating wavelength, Λ, without scattering and the initial decay rate is $\sim v_F q$, the reciprocal of the time required for an electron moving with the Fermi velocity to traverse a distance $\Lambda/2\pi$.

Although the grating's initial decay rate saturates near $v_F q$ when T reaches ~ 50 K, its time dependence continues to change as T is lowered further. Fig. 3.3 shows the grating amplitude as function of time for several temperatures between 5 K and 100 K, measured with a grating wavevector of 2.5×10^4 cm^{-1} (the T indicated is the lattice temperature, which is below the electron temperature, as discussed in Section 3.2.3). An oscillatory structure appears in the decay curves, becoming increasingly pronounced as T decreases. The growth of these oscillations is a consequence of the increase of the mean-free-path, l, in the regime where $ql \geq 1$.

To determine D_s from data such as those in Fig. 3.3 we use an expression for the time dependence of a spin fluctuation that is applicable throughout the diffusive-ballistic crossover regime. If a spin polarization wave is introduced at $t = 0$, its subsequent time-dependence is the Fourier transform of $S(q,\omega) \propto [i\omega - D(q,\omega)q^2]^{-1}$, where $D(q,\omega)$ is the dynamic spin diffusivity. In the limit $q \ll k_F$,

$$D(q,\omega) = \frac{v_F/2}{\sqrt{(i\omega/v_F - 1/l)^2 + q^2}}, \qquad (3.1)$$

where Eq. 3.1 extrapolates from the small-q limit[21] to the ballistic regime. In attempting to fit the grating decay curves in the "plateau" regime, we found that Eq. 3.1 is not quite sufficient to describe the data. It is necessary to add to the Fourier transform of $S(q,\omega)$ a small, slowly decaying exponential with relative initial amplitude ≈ 0.1 and characteristic time ≈ 25 ps. We speculate that this slow exponential may originate from a small fraction of localized electrons. The solid lines through the data points in Fig. 3.3 show the results of the fitting procedure, with fitting parameters l, v_F, and the amplitude and time constant of the slow exponential. Despite the complicating presence of the slow exponential, we believe that the fits give an accurate indication of l, as this is the only parameter that determines the rate at which the oscillations are damped. Finally, the spin diffusion coefficient is determined from the relation $D_s = v_F l/2$.

3.2.2 Comparison with D_{c0}

The temperature dependence of D_s obtained from our analysis of the spin-grating dynamics is shown in Fig. 3.4 for QW's of different electron density. For the two lower density samples (middle and lower panels), the dynamics were diffusive at all T, consistent with their lower mobility. To characterize charge transport in the same set of samples, we performed 4-probe measurements (Hall effect in the van der Pauw geometry) of the 2D charge conductance, σ_c, carrier density, n, and mobility, μ, on chips from the same set of wafers. Together, these measurements allow us to test the assumption that the scattering processes that control spin diffusion and charge conduction
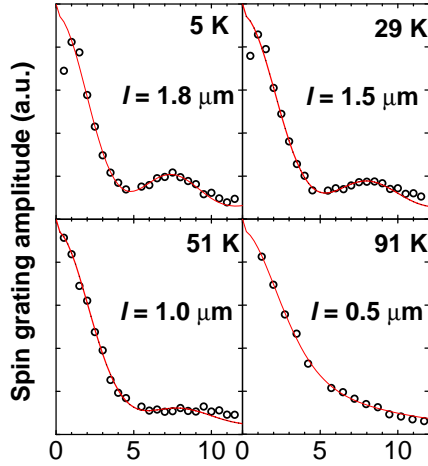
Figure 3.3. Time-dependence of the spin-grating's amplitude. The lines are fits of the data to the fourier transform of $S(q, \omega)$. The values of l determined from these fits are indicated in each panel. Due to laser heating, the temperature T_e of the electron gas is higher than the lattice temperatures indicated.

are the same. The link between conductance and diffusion coefficient is the Einstein relation, $D_s = \sigma_s/e^2\chi_s$, where σ_s and χ_s are the spin conductance and susceptibility, respectively. If the spin and charge scattering rates were the same (*i.e.* $\sigma_c = \sigma_s$), then D_s would equal $(\chi_0/\chi_s)D_{c0}$,[22] where $D_{c0} \equiv \sigma_c/e^2\chi_0$ and $\chi_0 = N_F(1 - e^{-E_F/k_BT})$ is the noninteracting susceptibility (see below; N_F is the density of states at the Fermi energy). Physically, D_{c0} is the quasiparticle diffusion coefficient[22], approaching $\mu E_F/e$ and $\mu k_BT/e$ in the degenerate and nondegenerate regimes, respectively. D_{c0}, calculated from the 4-probe transport data and plotted in Fig. 3.4, is considerably larger than D_s at all T and for each of the samples. The ratio is far greater than can be accounted for by many-body enhancement of the spin susceptibility, as the factor χ_s/χ_0 is less than 1.4 in this range of electron density, according to both analytical theory[23] and Monte Carlo simulations[24].

Derivation of χ_0

D_{c0} can be obtained directly from our 4-probe transport measurements, which determine σ_c, n, and therefore E_F. For a 2DEG, the noninteracting susceptibility χ_0 can be expressed in closed form in terms of the E_F, T, and the density of states, N_F, as we now describe. The starting point is the definition $\chi_0 \equiv \partial n/\partial\mu$, where the derivative of n with respect to chemical potential μ is for the noninteracting system. n and μ are related through the integral of the Fermi function,

$$n = N_F \int_0^\infty \frac{dE}{1 + e^{(E-\mu)/kT}}, \tag{3.2}$$

14

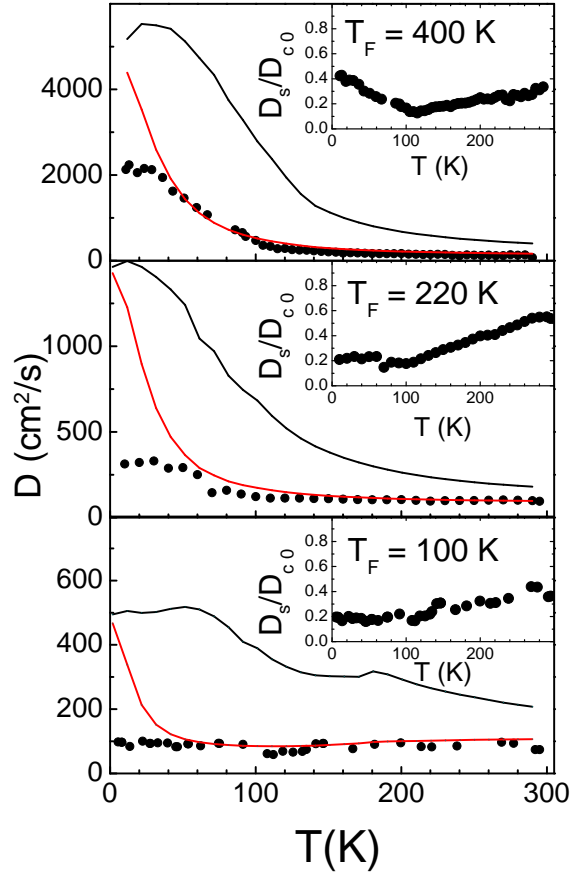Figure 3.4. Comparison of motion of spin and charge, for samples with the Fermi temperatures shown. **Dots (main panels):** Spin-diffusion coefficients D_s determined from optical measurements. **Upper lines:** Quasiparticle diffusion coefficients D_{c0} determined from transport data. **Insets:** D_s/D_{c0}. **Lower lines:** D_s predicted from spin Coulomb drag theory, taking $\chi_s = \chi_0$.

which can be evaluated analytically to obtain,

$$n = N_F k_B T \ln(1 + e^{\mu/kT}). \tag{3.3}$$

Taking the derivative of n with respect to μ yields the following expression for χ_0,

$$\chi_0 \equiv \frac{\partial n}{\partial \mu} = \frac{N_F}{1 + e^{-\mu/kT}}. \tag{3.4}$$

We can invert Eq. 3 to obtain μ in terms of $n = N_F E_F$ and substitute, getting:

$$\chi_0 = N_F(1 - e^{-E_F/k_B T}), \tag{3.5}$$

and

$$D_{c0} = \frac{\sigma_c}{e^2 N_F(1 - e^{-E_F/k_B T})}. \tag{3.6}$$

D_{c0}, expressed in other equivalent forms, has been used widely as an estimate for the spin diffusion coefficient expected when many-body renormalization of the spin susceptibility can be neglected. It has the familiar limits $v_F^2 \tau/2$ and $v_{th}^2 \tau/2$ in the degenerate and nondegenerate limits, respectively (v_F is the Fermi velocity, $v_{th} \equiv \sqrt{2k_B T/m^*}$ is the thermal velocity, and τ is the transport mean-free-time). The surprising conclusion of our measurements is that for high-electron-density, low-disorder 2DEG's, where many-body renormalization is expected to be very weak, electron-electron collisions nevertheless control D_s and reduce it well below D_{c0}.

Why we believe our measurement of ρ_c

We performed 4-probe measurements of resistivity and Hall effect as a function of T for each of the samples used in this study. We have strong evidence from the transport data that the electron density is quite uniform among the 10 QW's. In characterizing the samples, we can compare the average electron density (obtained by dividing by 10 the density obtained from transport) with the target density given by the number of Si atoms introduced into the barrier layer. This comparison is presented in a table in Fig. 3.5. As can be seen from the table, the electron density assuming each well is the same is very close to the target density. We believe the effects of varying density are not greater than 10% and that such effects cannot explain the discrepancy between spin and charge transport coefficients which differ by as much as a factor of 7. It is also worth noting that Si will act as a donor when it sits on a Ga site, and as an acceptor on an As site. According to Jason Stephens, it is very widely accepted among people who make GaAs quantum wells that Si dopants occupy Ga sites—consistent with the data shown in Fig. 3.5.

Sample name	$n/10$(from transport)	Target Si density
AW03 / AW07	$7.83 \times 10^{11} \mathrm{cm}^{-2}$	8×10^{11} cm $^{-2}$
AW09	$4.31 \times 10^{11} \mathrm{cm}^{-2}$	4×10^{11} cm $^{-2}$
AW12	$1.88 \times 10^{11} \mathrm{cm}^{-2}$	2×10^{11} cm $^{-2}$

Figure 3.5. Comparison of the average electron density (obtained by dividing by 10 the density obtained from transport) with the target density given by the number of Si atoms introduced into the barrier layer, for three samples.

3.2.3 Comparison of data with sCd theory

The contrast in the diffusion coefficients of charge and spin seen in Fig. 3.4 is surprising, as the assumption $D_s = D_{c0}$ is widely used in modeling spin transport in semiconductors. However, this assumption fails to take into account e-e collisions, whose rate can be much faster than those of impurity or phonon scattering. The e-e scattering events can be ignored in the description of charge transport because they conserve total momentum. However, they can have a profound effect on spin transport, as illustrated in Fig. 3.6. For the collision depicted between electrons with opposite spin, the charge current is conserved while the spin current reverses direction.

D'Amico and Vignale (DV) have proposed that the microscopic process shown in Fig. 3.6 can change the nature of macroscopic spin transport. Seen macroscopically, e-e collisions transfer momentum between the spin-up and spin-down populations, creating a force damping their relative motion that DV term "spin Coulomb drag" (sCd)[7] (by analogy with "Coulomb drag"; for a recent review see Rojo et $al.$[25]). Spin diffusion, which requires a counterflow of the spin populations, is damped by sCd, while charge diffusion is not. (The recently observed[26,27] spin Hall effect also involves the counterflow of spin populations, and so should be damped by sCd.) According to DV[7], the reduction of D_s relative to D_{c0} is:

$$\frac{D_s}{D_{c0}} = \left(\frac{\chi_0}{\chi_s}\right) \frac{1}{1 + |\rho_{\uparrow\downarrow}|/\rho},$$ (3.7)

where $\rho = 1/\sigma_c$ is the charge resistance and $\rho_{\uparrow\downarrow}$ is the spin drag resistance, parameterizing the rate of momentum exchange between spin $\uparrow$ and $\downarrow$ electrons. DV, and Flensberg and Jensen[28], have calculated $\rho_{\uparrow\downarrow}(T)$ for a 2DEG using the random phase approximation (RPA), obtaining results that depend only on the electron density of the quantum well.

Eq. 3.7 predicts that despite the complex T dependences of the individual diffusion coefficients, their ratio depends primarily on the single single factor, $|\rho_{\uparrow\downarrow}|/\rho$. We test this prediction in Fig. 3.7, without invoking any assumptions or adjustable parameters, by plotting D_{c0}/D_s (the inverse of Eq. 3.7) $vs.$ $|\rho_{\uparrow\downarrow}|/\rho$ for each of the three samples measured in this study. The transport coefficients are taken directly from our measurements, while $|\rho_{\uparrow\downarrow}|$ was calculated using Eq. 2 of D'Amico and
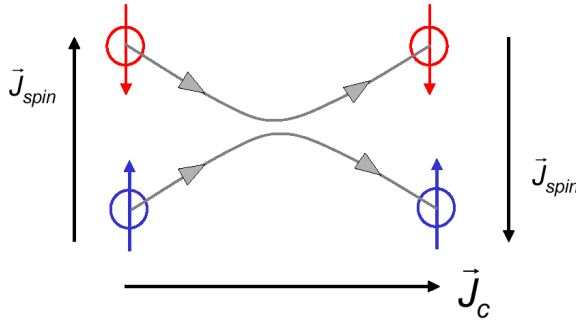
Figure 3.6. A representation of *e-e* scattering that does not conserve spin-current. Prior to the collision the spin-current is positive; after, it is negative. The charge current does not change.

Vignale[8]. The resulting graph reveals the simple linear dependence of D_{c0}/D_s on $|\rho_{\uparrow\downarrow}|/\rho$ predicted by Eq. 3.7 over a large range of $|\rho_{\uparrow\downarrow}|/\rho$, implying that sCd is indeed the origin of the large suppression of D_s relative to D_{c0}. The fact that the slope is slightly greater than unity is consistent with the expectation that the many-body enhancement of χ_s relative to χ_0 is small in this density regime.[23,24] Finally, the fact that D_{c0}/D_s extrapolates to near unity as $|\rho_{\uparrow\downarrow}|/\rho \to 0$ indicates that the spin and charge diffusion coefficients approach each other in the limit that the spin drag resistance becomes smaller than the ordinary resistance. This result provides independent evidence that the spin grating and four-probe techniques used in this work accurately measure equilibrium spin and charge transport coefficients, respectively.

Optical heating of electrons

Returning to the T-dependence shown in Fig. 3.4, the lower lines show the prediction of Eq. 3.7 for D_s with the factor χ_0/χ_s set equal to unity. As could be anticipated from the discussion of Fig. 3.7, sCd quantitatively accounts for the suppression of D_s relative to D_{c0} over a broad range of temperature and electron density. It is clear, however, that the measured D_s consistently departs from theory below 40 K. We believe that this discrepancy indicates that at low T the photoexcited electron gas does not cool to the lattice T. If the electron gas retains the heat, Q, deposited by the excitation, its temperature T_e will rise to approximately $(T^2 + 2Q/\beta)^{1/2}$, where $\beta = 5.3 \times 10^5$ eV/cm²-K^2 is the temperature coefficient of the electronic specific heat, calculated for free electrons in two dimensions. We estimate $Q = 4 \times 10^8$ eV/cm², assuming that each absorbed photon deposits approximately 10 meV (the energy width of the laser pulse) into the Fermi sea. The resulting estimate for the minimum T_e is indeed ~ 35 K.
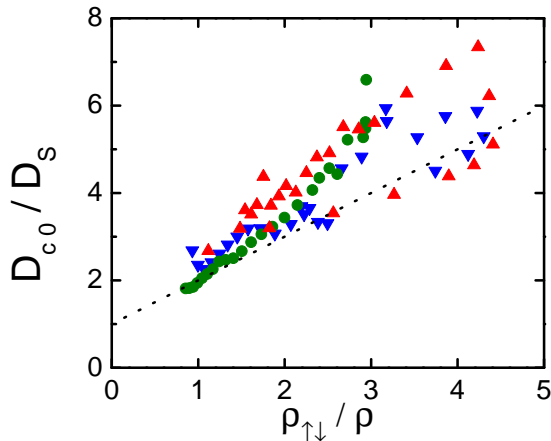
Figure 3.7. Relation between suppression of spin diffusion and spin drag resistance. **X-axis:** ratio of $\rho_{\uparrow\downarrow}$, determined from sCd theory[8], to measured resistivity ρ. **Y-axis:** ratio of quasiparticle diffusion coefficient, D_{c0}, to spin diffusion coefficient, D_s. Temperature is an implicit parameter. Points are for samples with $T_F = 400$ K (**triangles up**), 220 K (**circles**), and 100 K (**triangles down**). Points for $T < 40$ K are not shown because the electrons do not cool below 40 K. **Line:** has unity slope and intercept, indicating the prediction of Eq. 3.7 for $\chi_s = \chi_0$. For points above the line, $\chi_s > \chi_0$.

3.3 Results on other samples

3.3.1 Disordered samples

We originally had two reasons to be interested in measuring disordered samples. First is that we hoped they might put us on the track of the Burkov-MacDonald effect[29], which had been our "holy grail," or perhaps our "white whale." Second, they can provide a "control" experiment for our observation of spin Coulomb drag. Since D_s and D_{c0} are measured by different techniques, we would like to be sure that the observed suppression of D_s does not result from a systematic difference between the two experiments. In particular, in the limit that $|\rho_{\uparrow\downarrow}|/\rho \to 0$, D_s should approach D_{c0}. Since $\rho_{\uparrow\downarrow}$ is intrinsic to electron-electron scattering, one cannot "turn off" $\rho_{\uparrow\downarrow}$, except by lowering the electronic temperature, which is difficult due to laser heating. So we decided instead to increase ρ, by depositing a portion of the dopants (randomly distributed) in the quantum wells rather than in the Al-GaAs barrier layers.[30,31,32] This batch of samples was also the first batch in which we had some samples with 30 wells, rather than 10, for greater signal.

Jason Stephens sent us the first of these samples on 17 June 2005. At the time of this writing (November 2005), we have measured two of these: starting on 14 July, a sample with 30 wells and 33% of the dopant deposited in the wells (at room temperature, the carrier concentration is 7.9 $\times 10^{11}$ cm^{-2} per well); and starting on 21 July, a sample with 30 wells, 83% in the wells, and $n =$
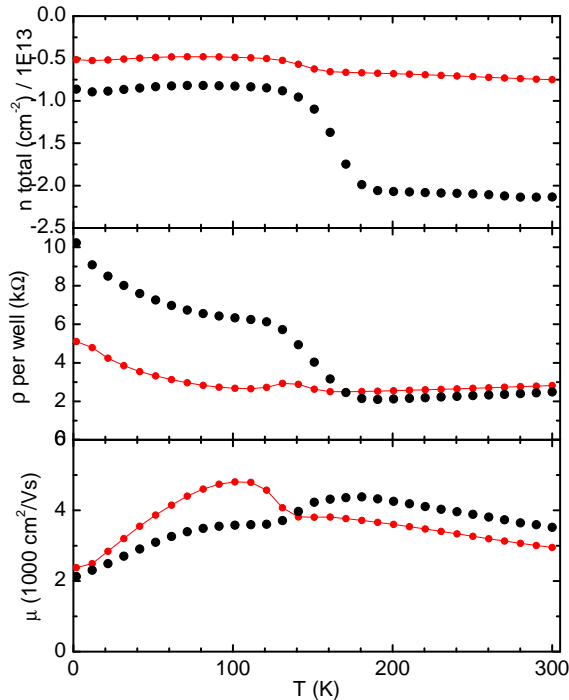
Figure 3.8. Transport data for the 100% sample (points with lines; has 10 wells) and 83% sample (points without lines; has 30 wells). The total n for all wells is shown. ρ shown is per well. Changes in the data below 175 K were even larger for the 33% and 17% samples.

7.9 $\times 10^{11}$ cm^{-2} per well. We do not trust all of the transport data for these samples; they seem to go bad below $\approx$ 175 K, we speculate perhaps because a contact may be freezing out. These transport data were obtained from Hall effect measurements in the van der Pauw geometry; we hope to measure the conductivity without contacts by THz spectroscopy. Data for the 100% and 83% samples appear in Fig. 3.8. The room temperature data, however, look very reasonable: the resistivity very nearly matches $\rho[\Omega] = 100\Omega + 2700\Omega \times \sqrt{p}$, where p is the portion of the dopant in the well (see Fig. 3.9).

The 33% sample we measured only at room temperature, finding $D_s = 108$ cm^2/s $\tau_s = 19.6$ ps, and $L_s = 0.46$ μm. The measured resistivity is 1770 Ω, and $\rho_{\uparrow\downarrow}$ is predicted to be 1320 Ω, so $D_{c0}/D_s = 1.96$ and $1 + |\rho_{\uparrow\downarrow}|/\rho = 1.75$. The agreement with sCd theory is fine, but it is surprising that L_s is so small (see Chapter 4).

For the 83% sample, we find that at room temperature, $D_s = 86$ cm^2/s, $\tau_s = 80$ ps, and $\rho = 2500$ Ω; the predicted $\rho_{\uparrow\downarrow}$ is 1350 Ω. Thus $L_s = 0.83$ μm and $D_{c0} = 150$ cm^2/s. If we assume sCd theory to be exact, these give $\chi_s/\chi_0 = 1.1$. This point, along with two other temperatures above 175 K, are the three additional (orange) points in Fig. 3.10. Temperature-dependent data for this sample appear in Fig. 3.11. Though these data are taken only from our optical measurements, and do not depend on the transport data, they, too, present some puzzles at lower temperatures.
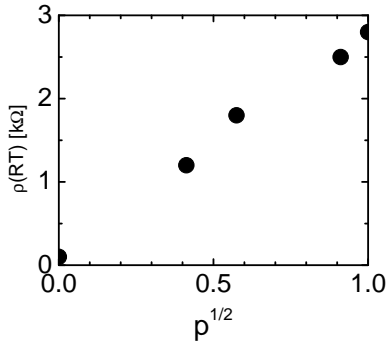
20

Figure 3.9. Room-temperature resistivity of five samples, *vs.* the square root of the portion p of the dopant atoms deposited in the quantum well (the remainder, $1 - p$, are deposited in the Al-GaAs barriers). All samples had $T_F \approx 400$ K.

First, the q-dependence at low T shows an anomalous dispersion, closer to $\gamma_q \sim q^3$ than to $\gamma_q \sim q^2$. Second, the low-T curves (transient-grating signal *vs.* time) show a "bounce" (or zero-crossing) that we do not think is related to a residual intensity grating. Analysis of this bounce complicates interpretation of $\gamma(q)$ and $\gamma(T)$. Finally, the spin-diffusion length, L_s, gets larger as T approaches zero, ending up around 2 μm. As explained in Chapter 4, we expect L_s to be nearly constant and roughly 1 μm, in keeping with the D'yakonov-Perel mechanism of spin relaxation[33].

3.3.2   (110) quantum wells

On 22 June, 2005, Hideo Ohno sent us two samples, both GaAs/Al-GaAs quantum wells grown in the (110) direction. Spin lifetimes in (110) QWs are much longer than in (100) wells[34] (see Chapter 4).

One sample, named VR420, had five wells with carrier density 1.3×10^{12} cm^{-2} each, and room-temperature resistivity $\rho(RT) = 2750$ Ω. The other, VR510, five wells with $n = 4 \times 10^{11}$ cm^{-2} each; we don't know $\rho(RT)$. Irene D'Amico sent us calculations for $\rho_{\uparrow\downarrow}(T)$ for these two values of n, giving room temperature values of 644 Ω and 2620 Ω, respectively.

I cracked the substrate of the first sample, leaving a sample that is probably fine for optical measurements (I was able to see a weak transient-grating signal in intensity-mode) but is unsuitable for low-temperature measurements in a cold-finger cryostat. (Nonetheless, I took some data around 175 K.) At room temperature, I found a q^2 dispersion, $D_s \approx 53$ cm^2/s, and γ_s indistinguishable from zero. So $D_{c0}/D_s = 2.13$, and $|\rho_{\uparrow\downarrow}|/\rho = 0.23$, which is not particularly good agreement with sCd theory. Because of the lack of transport data, I never measured VR510.
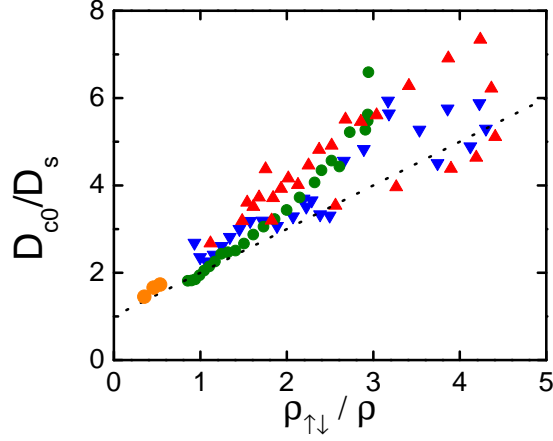
Figure 3.10. The same data as shown in Fig. 3.7, with three additional points. These points are for the sample with $T_F = 400$ K and 83% of the dopant deposited in the well, and are for temperatures above 175 K, where we believe the transport data are reliable. The fact that D_{c0}/D_s extrapolates to near unity as $|\rho_{\uparrow\downarrow}|/\rho \to 0$ indicates that the spin and charge diffusion coefficients approach each other in the limit that the spin drag resistance becomes smaller than the ordinary resistance.
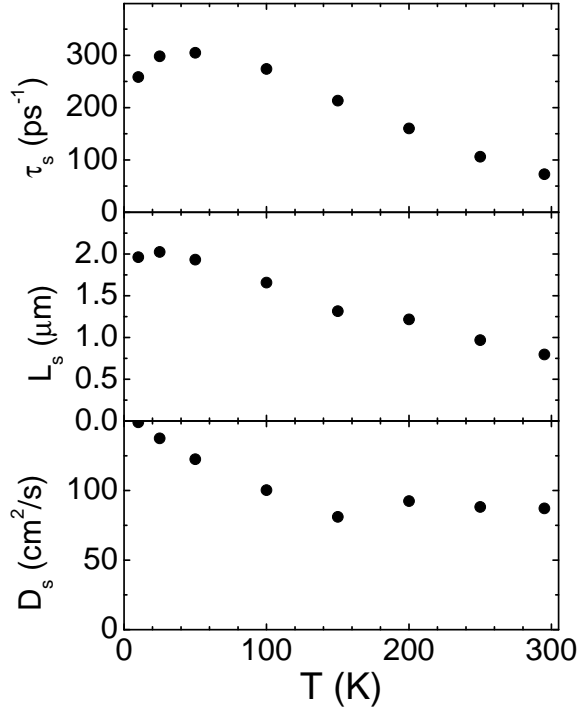
Figure 3.11. Temperature-dependent data for the same disordered sample that provided the additional points in Fig. 3.10. L_s is calculated from $\sqrt{\tau_s D_s}$.

3.3.3 The old Chemla sample

Before measuring quantum wells, we had tried to measure spin diffusion in bulk GaAs samples, thinned by mechanical polishing so that we could do measurements in transmission rather than reflection. (Many thanks to Ben Cardozo of Eugene Haller's group for his help with the polishing!) However, we observed features that puzzled us, that we speculated might be related to the Franz-Keldysh effect[35,36] due to the surface field. So we decided to try measuring a quantum well.

Our first quantum-well sample was borrowed from Daniel Chemla's group on 9 February, 2004. It was a sample that Neil Fromer had used in his thesis work, grown by Dan Driscoll in Art Gossard's group at UC Santa Barbara[37]. We named this sample CW01; Fromer's name for it was D00707. It consists of 10 quantum wells of thickness 12 nm, separated by 42 nm $Al_{0.3}Ga_{0.7}As$ barriers, with $n \sim 2 \times 10^{11}$ cm^{-2} each. The carriers were modulation-doped: the Si donors were deposited in the central 12 nm of the barriers. This sample was the pattern for the first batch of quantum wells that Jason Stephens grew for us[6], which includes all three non-disordered samples mentioned above (Stephens was able to find Driscoll's detailed "recipe" for the sample).

We don't know $\rho(T)$, but do know that at room temperature and 5 K, the mobility is $\mu = 4 \times 10^3$ cm^2/V-s and $\mu = 9 \times 10^4$ cm^2/V-s, giving $\rho = 7.8$ kΩ and 350 Ω, respectively. Our optical measurements gave $D_s(RT) = 88$ cm^2/s and $D_s(5K)$ somewhere between 35 and 80 cm^2/s. This gives $D_{c0}/D_s = 1.4$ and $|\rho_{\uparrow\downarrow}|/\rho = 0.62$ at room temperature, which agrees fairly with sCd theory. At 5 K D_{c0}/D_s is between 10 and 23 and $|\rho_{\uparrow\downarrow}|/\rho = 0.68$.

Chapter 4

Spin Relaxation

4.1 Introduction

The spin-orbit coupling in semiconductors such as GaAs has been proposed as a mechanism for control of spin[1], but it also can contribute to spin relaxation. Here I describe our experiments exploring the mechanism of spin relaxation in two-dimensional electron gases in both the degenerate and the nondegenerate regimes.

To investigate spin relaxation, we measured the same three non-disordered quantum well (QW) samples as we used for our measurements of D_s, discussed in Chapter 3. We measured τ_s independently of D_s through the decay of circular dichroism[20,10]: a circularly polarized pump-beam excites spatially homogenous spin polarization, which results in circular dichroism; a time-delayed probe pulse has circular polarization either the same as (SCP) or opposite to (OCP) that of the pump. The transient changes in transmitted intensity of the SCP and OCP cases are subtracted, giving the time-dependence of the spin polarization, from which we determine τ_s. The operation of the laser and the optical heating of the electron gas are the same as in the diffusion measurements.

The unfortunate nature of this field is that the few simple results follow from a long chain of calculations and approximations. Indeed, the content of the theory is summed up in Eqs. 4.10 and 4.16, and the experimental content in Fig. 4.2. I include a detailed account of the theory, of prior experiments, and of the long history of misinterpreting the theory, in order to highlight the new features of this experiment, as laid out in Section 4.2.

4.1.1 Explanation of D'yakonov-Perel'-Kachorovskii spin relaxation

Spin relaxation in these systems is believed to be dominated by the D'yakonov-Perel'-Kachorovskii (DPK) mechanism of precessional dephasing in the spin-orbit field[15]. Each electron experiences an "effective magnetic field" that depends on its wavevector $\mathbf{k}$, causing its spin to precess about an effective Larmor vector $\mathbf{\Omega}(\mathbf{k})$. Each time an electron is scattered, its $\mathbf{\Omega}$ also scatters. If the spins precess through an angle much less than 2π between events that scatter $\mathbf{k}$ (the "motional narrowing" regime), then the frequent scattering of the precession axis $\mathbf{\Omega}$ causes the spin's direction to execute a random walk in angle-space. The net effect on a spin population is, surprisingly, that increasing the scattering rate *lengthens* τ_s.

Three dimensions

We start by defining a set of electronic scattering times, τ_l. Using the notation of Pikus and Titkov[11], for electrons of energy ε:

$$\frac{1}{\tau_l(\varepsilon)} = N(\varepsilon) \int \frac{d\omega}{4\pi} W(\varepsilon, \theta) \left[1 - P_l\left(\cos\theta\right)\right], \tag{4.1}$$

Here $W(\varepsilon, \theta) \cdot \delta(\varepsilon - \varepsilon')$ is the probability of scattering through an angle θ, $N(\varepsilon)$ is the density of states, the integral over $d\omega$ is over the unit sphere, and θ is the polar angle. P_l is the lth (odd) Legendre polynomial; for even l, $1/\tau_l = 0$. D'yakonov and Perel'[33] find that τ_3 controls the spin relaxation. In the motional narrowing regime, the spin lifetime becomes:

$$\frac{1}{\tau_s} = \frac{2}{3} \left\langle \overline{\Omega^2} \tau_3 \right\rangle, \tag{4.2}$$

where $\overline{\Omega^2}$ is an average over angles, and $\langle \cdot \rangle$ is an average over energy. It would be convenient, however, to express τ_s in terms of a parameter more experimentally accessible than τ_3. For this reason D'yakonov and Perel' consider the "momentum scattering time" of a single electron, $\tau_{\mathbf{p}} = \tau_1$:

$$\frac{1}{\tau_{\mathbf{p}}(\varepsilon)} = N(\varepsilon) \int \frac{d\omega}{4\pi} W(\varepsilon, \theta)[1 - \cos\theta]. \tag{4.3}$$

As mentioned in Chapter 3, the scattering time for the *total* electronic momentum, which determines the resistivity, does not include the effect of *e-e* collisions. For this reason $\tau_{\mathbf{p}}$ is not quite as experimentally accessible as is sometimes supposed—at least, it cannot be inferred directly from transport measurements. Moreover, the relation between $\tau_{\mathbf{p}}$ and τ_3 depends on the θ-dependence of the scattering mechanism. For scattering off of acoustic phonons $\tau_3 = \tau_{\mathbf{p}}$, while for scattering off of ionized impurities or holes $\tau_3 = \tau_{\mathbf{p}}/6$. The distinction, then, between τ_3 and $\tau_{\mathbf{p}}$ can strongly influ-

ence the spin relaxation time, as can the difference between contributions from different scattering mechanisms.

Two dimensions

In a quantum well of a zincblende material, the spin-orbit Hamiltonian takes the form[38]

$$H_{SO} = \frac{\hbar\alpha_R}{2}\left(k_y\sigma_x - k_x\sigma_y\right) + \frac{\hbar\alpha_D}{2}\left(k_y\sigma_y - k_x\sigma_x\right). \tag{4.4}$$

Here $\hat{z}$ is the growth direction, and α_R and α_D are the Rashba and Dresselhaus coefficients. The magnitude of the $\boldsymbol{\Omega}$ resulting from combined Rashba and Dresselhaus coupling scales as $\sim |\mathbf{k}|$, but both its magnitude and its direction depend on the direction of $\mathbf{k}$. The Dresselhaus coupling also scales as

$$\begin{aligned} \Omega_D &\sim \alpha_D \\ &\sim q^2 \\ &\sim E_{1e}, \end{aligned} \tag{4.5}$$

where q is the wavevector in the growth direction and E_{1e} is the confinement energy. The Dresselhaus term arises from the bulk inversion asymmetry of the zincblende structure, while the Rashba term arises from asymmetry along the growth direction of the QW. For this reason it is usually assumed that for nominally symmetric wells $\boldsymbol{\Omega}$ is dominated by the Dresselhaus term. In fact, Eq. 4.4 gives $\boldsymbol{\Omega}$ only perturbatively. Further possible refinements include adding a Dresselhaus term that scales as k^3/q^2 or even performing non-perturbative calculations in a fourteen-band basis[39]. Writing $\Omega_{j,l}$ for the coefficients of expanding the jth vector component of $\boldsymbol{\Omega}$ in the basis of $\cos(l\theta)$, $\sin(l\theta)$,

$$\Omega_j(\theta) = \sum_l \Omega_{j,lc}\cos(l\theta) + \Omega_{j,ls}\sin(l\theta), \tag{4.6}$$

we can define

$$\Omega_l^2 = |\boldsymbol{\Omega_{lc}}|^2 + |\boldsymbol{\Omega_{ls}}|^2. \tag{4.7}$$

Then defining τ_l in analogy with the 3-D case,

$$\frac{1}{\tau_l(\varepsilon)} = N(\varepsilon)\int_0^{2\pi} d\theta W(\theta,\varepsilon)[1 - \cos(l\theta)]. \tag{4.8}$$

Again $\tau_{\mathbf{p}} = \tau_1$, and again τ_l depends on the scattering mechanism. Then

$$
\begin{aligned}
\frac{1}{\tau_s} &= \frac{1}{n} \int d\varepsilon N(\varepsilon) f(\varepsilon) \left[1 - f(\varepsilon)\right] \sum_l \tau_l(\varepsilon) \Omega_l^2(\varepsilon) \\
&= \sum_l \left\langle \tau_l \Omega_l^2 \right\rangle,
\end{aligned}
\tag{4.9}
$$

where n is the electronic density and $\langle \cdot \rangle$ is the thermal average indicated. For a (100) QW, the out-of-plane component of the spin, S_z, relaxes with $\tau_z = \tau_s$, while the in-plane component relaxes with $2\tau_s$. All of the optical measurements discussed here, both in this work and in previous work, measure $S_z(t)$.

Some preferred approximations of the DPK relation

It is evident that deriving quantitative predictions from Eq. 4.9 will require a number of approximations. The approach we take here is roughly equivalent to that most commonly found in the literature.

Using perturbative expressions for Ω_D, for a (100) QW one gets $\Omega_{D,3} \sim k^3$, which is the same as in three dimensions. However, while in three dimensions $\Omega_{D,1} = 0$, in two dimensions $\Omega_{D,1} \sim k E_{1e}$. Thus if Dresselhaus coupling exists, as it is certain to, then there will be a term $\Omega_{D,1}$ of order k. The Rashba coupling also has an $l = 1$ component; so regardless of the relative strength of the two couplings the $l = 1$ term should dominate the spin relaxation:

$$
\frac{1}{\tau_s} = \left\langle \tau_{\mathbf{p}} \Omega_1^2 \right\rangle.
\tag{4.10}
$$

A widely repeated result of Eq. 4.10 is that τ_s^{-1} is proportional to the mobility, μ, independent of the dominant scattering mechanism. This result, however, is based on the mistaken belief that $\mu \propto \tau_{\mathbf{p}}$. In fact, scattering that preserves the *total* electronic momentum (such as *e-e* collisions) contributes to μ only weakly, through Umklapp processes, but contributes strongly to $\tau_{\mathbf{p}}$.

Next we use the perturbative expression for H_{SO} that gives $|\mathbf{\Omega_{D,R}}| = \alpha_{D,R} k$ to first order in k. Evaluating $\Omega_1^2(\varepsilon)$ requires knowledge of the relative strengths of α_D and α_R; but no such knowledge is needed to write $\Omega_1^2(\varepsilon) = \alpha_{\mathrm{eff}}^2 k^2(\varepsilon) = 2\alpha_{\mathrm{eff}}^2 m^* \varepsilon / \hbar^2$. The parameter α_{eff} is of order $\alpha_{D,R}$; since it depends only on $\alpha_{D,R}$, it should be a constant for a given quantum well structure. Because all of our QWs were grown with the same recipe, merely changing the dopant concentration, we believe that all of our wells have the same value of α_{eff}. We have, then,

$$
\frac{1}{\tau_s} = \frac{2\alpha_{\mathrm{eff}}^2 m^*}{\hbar^2} \left\langle \varepsilon \tau_{\mathbf{p}} \right\rangle
\tag{4.11}
$$

27

4.1.2 Prior work on spin relaxation in GaAs quantum wells

According to Eq. 4.10, τ_s depends on Ω, T, and $\tau_\mathbf{p}$. Though not discussed above, it also depends on the quantum well orientation[40]. Studies of DPK relaxation in GaAs QWs have accordingly taken the form of varying one or more of these four parameters. While studies *vs.* orientation have produced the results expected from DPK theory, studies *vs.* well width (changing Ω) and scattering rate have had much more limited success.

τ_s *vs.* quantum well orientation

One striking result of DPK theory is that in a (110) quantum well the out-of-plane spin component S_z does not decay, to first order. (The cubic Dresselhaus term can still cause S_z to relax.) Hideo Ohno's group[34,41,42] investigated τ_s in both (100) and (110) QWs, finding that $\tau_s^{(110)}$ exceeded $\tau_s^{(100)}$ by a factor of 30 or more. This slow rate, moreover, did not appear to originate from the DPK mechanism, as indicated by their studies of $\tau_s^{(110)}$ as a function of temperature and well width. (Admittedly, though, the same trends in $\tau_s^{(100)}$ were only partially consistent with DPK; see below.) For undoped (110) wells they speculated that spin relaxation might be due to the electron-hole exchange interaction[43]. Measurement of n-doped (110) QWs supported this conclusion: $\tau_s^{(110)}$ was yet longer than in the undoped samples, as expected due to screening of the electron-hole interaction[42].

τ_s *vs.* well width

If Dresselhaus coupling is assumed to be stronger than Rashba (which is *not* assumed in Eq. 4.10), then Eq. 4.5 predicts that $\tau_s \sim E_{1e}^{-2}$ which depends on the QW's width. Tackeuchi *et al.*[44] measured τ_s for a series of undoped wells of various widths at room temperature. They found agreement with E_{1e}^{-2}, though over the rather restricted range of 80 meV $< E_{1e} <$ 160 meV. Subsequent work by Britton *et al.*[45] found that τ_s at low E_{1e} saturated around the bulk value of 50–100 ps, while at 160 meV τ_s was $\sim 35\%$ lower than found by Tackeuchi *et al.*—overall, a much weaker trend than E_{1e}^{-2}. Terauchi *et al.*[31] studied n-doped QWs (though still at room temperature), again finding τ_s to vary more weakly than E_{1e}^{-2}.

The first convincing trend, a good fit to $\tau_s^{-1} = .015$ ps$^{-1} + bE_{1e}^2$, was found by Malinowski *et al.*[46] in undoped QWs on 10–100 meV. Reviewing the various data from a theoretical perspective, Bournel *et al.*[47] optimistically deemed the agreement with E_{1e}^{-2} good, but remarked that the predicted values of τ_s were too short, by a factor from two[45] to ten[31]. This quantitative discrepancy between theory and experiment has been explored most thoroughly, though, not in studies of well width, but in studies of the scattering rate.

τ_s vs. temperature and scattering rate

Eq. 4.10 is commonly evaluated in the nondegenerate limit to give $\tau_s^{-1} \propto \tau_\mathbf{p}T$, which in turn is widely believed to predict that $\tau_s^{-1} \propto \mu T$. This prediction has inspired a series of experimental and theoretical studies of the μ- and T-dependence of τ_s. All of the measurements discussed here were on (100) QWs.

Terauchi *et al.*[31] studied a series of QWs of different mobilities at room temperature (RT). In order to vary the samples' mobility, some were modulation-doped with Si, while others were Si-doped in the well, or had both Be (an acceptor) and Si doped into the well. They found that each set of samples could fit to $\tau_s \propto \mu^{-1}$ over a narrow range of μ, but that taken as a whole the series of samples gave a much weaker dependence. More striking, though, was that their τ_s was longer than the DPK prediction by a factor of 5. A subsequent study by Ohno *et al.*[41] measured both $\tau_s(T)$ and $\mu(T)$ for a single sample with $n = 4 \times 10^{10}$ cm^{-2}. They found $\tau_s^{-1} \propto \mu T$ in the range from RT to 30 Kelvin—and quantitative agreement with the DPK prediction, provided they multiplied the predicted τ_s by a factor of 10. Malinowski *et al.*[46] measurred undoped wells of varying widths from 80 to 300 K, and found that for each one $\tau_s(T)$ was constant; this, they concluded, indicated that $\mu \propto T^{-1}$.

Reviewing the data from Terauchi *et al.*[31], Lau, Olesberg, and Flatté[39] concluded that neither $\tau_s \propto \mu^{-1}$ nor $\tau_s \propto E_{1e}^{-2}$ was consistent with the data. They introduced a detailed calculation that follows more or less the DPK model—τ_s given by Ω and $\tau_\mathbf{p}$ in a motional narrowing regime, Dresselhaus coupling assumed to be much stronger than Rashba—but that calculates $\Omega_l(\varepsilon)$ non-purturbatively in a 14-band basis. Their results agree much better with the data than do the DPK-based calculations in Terauchi *et al.*[31]: their τ_s are longer by about the needed factor of 5. If one supposes that as μ drops the scattering shifts from optical-phonon to nonionized-impurity, the calculated dependence on μ becomes weaker than μ^{-1}; and the calculated dependence on confinement energy is weaker than E_{1e}^{-2}.

Lau *et al.*'s calculation assumed that e-e scattering was "negligible in τ_l." Glazov and Ivchenko[48] treated the case of e-e scattering in a nondegenerate, (100) QW with Rashba coupling. They started with the scattering rate for exchange of energy among electrons: $\tau_{ee}^* = \hbar k_B T \epsilon^2 / ne^4$, where ϵ is the dielectric constant. They then calculated that $\tau_s^{-1} = I |\mathbf{\Omega}|^2 \tau_{ee}^*$, and found $I \approx 0.028$. (The value of I would likely be different under Dresselhaus coupling.)

Brand *et al.*[49] measured the spin polarization $S_z(t)$ for a high-mobility n-GaAs QW. At low temperature they observed time-dependences that oscillated and were damped; at increased T these crossed over smoothly to exponential relaxation. The oscillations, they realized, were the spin-orbit precession *outside* the motional narrowing regime, that is with $\Omega\tau_\mathbf{p} \gtrsim 1$. They used Monte Carlo simulations to extract $\tau_\mathbf{p}$ from these data, and also found the transport scattering time τ_μ from the mobility. At low T, $\tau_\mathbf{p}$ and τ_μ approached each other; but for 20 K $< T <$ 100 K, $\tau_\mathbf{p}$ was shorter than τ_μ by more than an order of magnitude. They postulated that this extra scattering

was due to e-e collisions, which should disappear as $T \to 0$. Calculating $\tau_{ee} \approx 1$ ps at 35 K from Fermi liquid theory, they confirmed that $\tau_{\mathbf{p}}^{-1} = \tau_{ee}^{-1} + \tau_\mu^{-1}$. However, to match this formula at other temperatures required $\tau_{ee} \sim T^{-1}$, which is not given by theory.

4.2 The strategy of this work

The key prediction of DPK theory is that in the motional narrowing regime $\tau_s^{-1} \propto \tau_{\mathbf{p}}$. To date comparisons between τ_s and $\tau_{\mathbf{p}}$ have been indirect, mostly inferring $\tau_{\mathbf{p}}$ from the mobility, *i.e.* assuming $\tau_{\mathbf{p}} = \tau_\mu$ and ignoring the effect of e-e scattering. The Monte Carlo simulations of Brand *et al.* do give $\tau_{\mathbf{p}}$ in the non-narrowed regime; but when the spin dynamics cross over to an exponential decay their method of inferring $\tau_{\mathbf{p}}$ amounts to *assuming* the DPK result. Agreement with $\tau_{\mathbf{p}}^{-1} = \tau_{ee}^{-1} + \tau_\mu^{-1}$ could test this assumption; but the agreement is good at only one temperature. (There is, however, one measurement in bulk GaAs for which $\tau_{\mathbf{p}}$ was determined independently through the dependence of τ_s on an applied magnetic field[50].)

To date no comparison has been made between measurements of τ_s and of D_s. We have found[6], for the n-doped, (100) QW samples we measured, that over a wide range of n and T the spin diffusion coefficient is given by D'Amico and Vignale's formula[8]:

$$\frac{D_s}{D_{c0}} = \left(\frac{\chi_0}{\chi_s}\right) \frac{1}{1 + |\rho_{\uparrow\downarrow}|/\rho}, \qquad (4.12)$$

which includes the effect of e-e scattering through the spin Coulomb drag term. We can thus infer $\tau_{\mathbf{p}}$ from D_s, as explained in Section 4.2.1. By measuring τ_s independently, we can test the prediction $\tau_s \propto \tau_{\mathbf{p}}^{-1}$; or, equivalently, that the spin diffusion length $L_s \equiv \sqrt{D_s \tau_s}$ is a constant[51] independent of n and T (see below). The new features of this work are: that it includes the effect of e-e collisions not as an inference, as in Brand *et al.*, but through the measured effect on D_s due to the spin Coulomb drag mechanism; and that it compares τ_s with a $\tau_{\mathbf{p}}$ that is not incorrectly inferred from the mobility.

4.2.1 Relating D_s to spin relaxation

The charge and spin diffusion coefficients, D_{c0} and D_s, can be understood in terms of the charge and spin conductivities, σ_c and σ_s, in a model-independent way through the Einstein relations: $D_{c0} = \sigma_c/\chi_0$ and $D_s = \sigma_s/\chi_s$. The scattering time that one infers from the conductivity (or mobility) is $\tau_\mu = \sigma_c m^*/ne^2$. We define an analogous "spin-scattering time" derived from the spin conductivity:

$$\tau_s' \equiv \sigma_s m^*/ne^2. \qquad (4.13)$$

The $'$ serves to distinguish this scattering time from the spin population lifetime, τ_s—two quantities that not only differ in magnitude but also have completely different meanings.

(As an aside on what this definition means, we note that Eqs. 4.12 and 4.13 imply that

$$\frac{1}{\tau_s'} = \frac{1}{\tau_\mu} + \frac{ne^2 |\rho_{\uparrow\downarrow}|}{m^*}. \tag{4.14}$$

Which says that, at least phenomenologically, $|\rho_{\uparrow\downarrow}|$ can be interpreted as adding another scattering mechanism to those that determine the mobility. Since $|\rho_{\uparrow\downarrow}|$ is the result of Coulomb interactions among electrons, one expects it to be closely related to τ_{ee}^{-1}.)

Returning to the relation of D_s to $\tau_\mathbf{p}$, the key step is to guess that $\tau_s' = a\tau_\mathbf{p}$, where a is a constant of order unity. This guess makes physical sense because the spin Coulomb drag theory does not involve spin-flip scattering. Roughly speaking, one can picture the spins as simply being carried on the electrons, with the resultant spin-current changing each time an electron's $\mathbf{k}$ scatters. In such a simple picture the spin transport should weight scattering through θ with $[1 - cos(\theta)]$, which is the same weighting as determines $\tau_\mathbf{p}$.

This guess, then, gives us a way of inferring $\tau_\mathbf{p}$ from D_s. The prediction we wish to test is that $\tau_s \tau_\mathbf{p} = $ const. This can be re-cast in terms of the spin diffusion length, $L_s \equiv \sqrt{D_s \tau_s}$. From Eqs. 4.11 and 4.13:

$$\begin{aligned} L_s^2 &= \frac{ane^2\hbar^2}{2\alpha_{\text{eff}}^2 m^{*2}} \frac{\tau_\mathbf{p}}{\chi_s \langle \tau_\mathbf{p}\varepsilon \rangle} \\ &= abn \left(\frac{\chi_0}{\chi_s} \right) \frac{\tau_\mathbf{p}}{\chi_0 \langle \tau_\mathbf{p}\varepsilon \rangle} \end{aligned} \tag{4.15}$$

Where $b = e^2\hbar^2/2\alpha_{\text{eff}}^2 m^{*2}$ is constant. Evaluation of the thermal average gives $\langle \varepsilon \rangle = E_F/\left(1 - e^{-E_F/k_B T}\right) = n/\chi_0$, so if we make the (admittedly rather bold) approximation that $\tau_\mathbf{p}(\varepsilon)$ is a constant, then

$$L_s^2 = ab\frac{\chi_0}{\chi_s}. \tag{4.16}$$

That is, L_s is constant. Reviewing what goes into this equation: a is the coefficient of the hypothesized relation between τ_s' and $\tau_\mathbf{p}$, which we expect to be a constant of order unity; b depends only on α_{eff}, which in turn depends on the quantum well structure but not on temperature or dopant level; and for 2DEGs of these densities and in this range of temperature, $1 < \chi_s/\chi_0 \lesssim 1.4$ (see Chapter 3). We have not explored the temperature dependence of χ_s/χ_0, but from Fig. 3.7 it appears that the temperature dependence is weak.
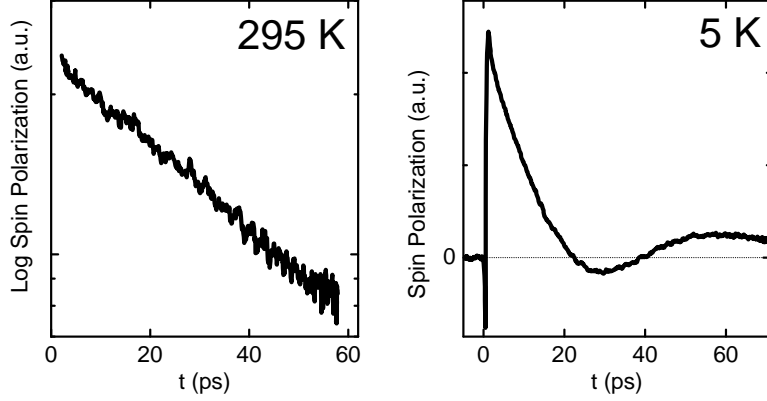
Figure 4.1. **Left:** Time-dependence of the photoinduced spin polarization at room temperature for the sample with $T_F = 400$ K, on a logarithmic scale. Drawing a straight line through the data gives an exponential decay with $\tau_s = 56$ ps. **Right:** Time-dependence of the photoinduced spin polarization of the same sample at 5 K, on a linear scale.

4.3 Results and discussion

The left panel of Fig. 4.1 shows the time-dependence of the induced spin polarization at room temperature for the sample with $T_F = 400$ K. The spin decays as a single exponential, with rate $\tau_s^{-1} = 0.018$ ps^{-1}. Most of the values of τ_s^{-1} determined in this experiment resulted from an exponential fit to the initial decay of a curve similar to that shown. However, in the most heavily doped sample at low temperature (where the mobility is high and e-e scattering is weak), the time-traces resemble the right panel of Fig. 4.1, with oscillations resulting from the precession of the spins in the spin-orbit field[49]. These two behaviors correspond to the diffusive and ballistic regimes of spin propagation found in the transient-grating experiments. In this work we discuss only our results in the diffusive regime.

Fig. 4.2 shows the values of D_s and τ_s^{-1} that we measured for these three samples. The diffusion coefficients all start out near 100 cm^2/Vs at room temperature. In the two more heavily doped samples, D_s rises (as does the mobility) as the temperature is lowered. The values of τ_s^{-1} show a similar pattern: the three samples have similar spin-relaxation times of ~ 75 ps^{-1} at room temperature, and diverge from each other at low temperatures. In fact, plotted on logarithmic axes, the curves for τ_s^{-1} look essentially like those of D_s, but with an overall "dip" around 100 K.

The right panel of Fig. 4.2 shows the spin diffusion length, L_s, calculated from $L_s = \sqrt{D_s \tau_s}$. We wish to emphasize three observations about these curves. First, the values of $L_s(T)$ for all three samples lie on top of each other: the diffusion length is insensitive to T_F. Second, L_s is nearly constant in temperature. Each panel of Fig. 4.2 is logarithmic, and covers two orders of magnitude. It is striking that, although D_s and τ_s^{-1} vary over most of that range, $\sqrt{D_s \tau_s}$ varies by at most a factor of two. This variation is our third observation: $L_s(T)$ curves downward, with a maximum
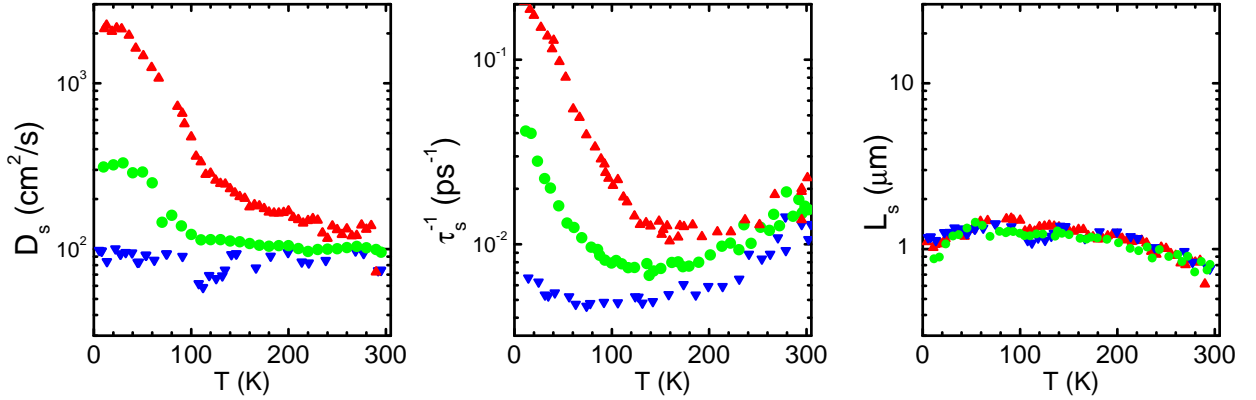
32

Figure 4.2. D_s, τ_s^{-1} and L_s for the samples with (top to bottom) $T_F = 400$ K, 220K and 100 K. Data in the left panel are taken from our optical measurements of the transient spin grating, Chapter 3. We obtain τ_s^{-1} from the decay of induced circular dichroism; L_s is calculated from $\sqrt{D_s \tau_s}$. The vertical axis of each panel covers two orders of magnitude. Notice that although D_s and τ_s^{-1} vary over most of that range, L_s is nearly a constant 1 μm at all temperatures and for all three dopings. The slight downward curve in $L_s(T)$ appears to be independent of doping.

around 100 K. The shape of this curve is the same for all three samples, and so is independent of T_F.

The basic conclusion to be drawn from these data is, from the constancy of L_s, that $\tau_s^{-1} \propto \tau_\mathbf{p}$, in keeping with the DPK prediction. The same data appear in Fig. 4.3 with temperature an implicit parameter. I show this plot primarily to emphasize the broad range of τ_s' over which our result holds. Though deviations from $\tau_s^{-1} \propto \tau_\mathbf{p}$ are apparent both in this figure and in the right panel of Fig. 4.2, the quantitative agreement is far better than in any of the studies that have compared τ_s to μ; indeed, it is comparable to the agreement that Lau *et al.* obtain through a detailed, non-perturbative calculation of $\Omega_l(\varepsilon)$.

What can we learn from the the data's *deviations* from the DPK prediction? First, the total spread in L_s is about a factor of 2. Considering the many approximations that went into the prediction, such a spread is hardly surprising; it also is not obvious which approximation is breaking down. However, the net spread in L_s at any one temperature, as a function of n (*i.e.*, for the three samples) is much less. Apparently, then, the approximations that lead to L_s's constancy in n are not breaking down: namely, that $\Omega_1^2 \propto \varepsilon$, and that D_s and $\langle \tau_\mathbf{p} \varepsilon \rangle$ both scale linearly with n.

We have seen, then, that the DPK theory's prediction $L_s(n, T) = const$ does indeed hold over a broad range of n and T—provided that one accounts for *e-e* collisions. The ratio D_{c0}/D_s, which is determined by the electrons' Coulomb interaction, is effectively a gauge of the importance of these

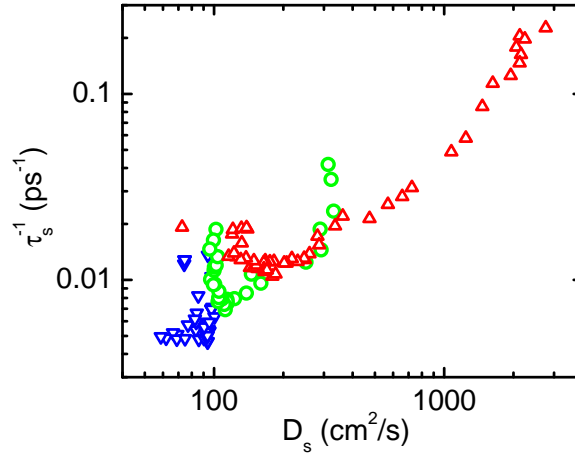Figure 4.3. τ_s^{-1} *vs.* D_s for the same three samples as in Fig. 4.2. Temperature is an implicit parameter, which generally decreases with increasing D_s. Each axis of the graph covers two orders of magnitude.

collisions. Considering that (Fig. 3.7) D_{c0}/D_s can be larger than 7.5, *e-e* collisions may often be the most important process determining the spin relaxation rate.

Chapter 5

Conclusion

This work has emphasized the role of *e-e* collisions in the transport and relaxation of spin. The primary finding is that the theory of spin Coulomb drag quantitatively describes spin transport over a broad range of n and T. Over much of that range, sCd suppresses spin diffusion by a large factor relative to charge diffusion, indicating that spin transport is largely controlled by *e-e* interactions.

Over the same range of n and T, spin relaxation follows the D'yakonov-Perel'-Kachorovskii model of interrupted precessional dephasing in the spin-orbit field. In particular, the relaxation's agreement with the DPK prediction that $\tau_s^{-1} \propto \tau_{\mathbf{p}}$ is much better than in previous studies that sought to relate τ_s to the mobility. The reason is essentially the same: mobility, like charge diffusion, is insensitive to *e-e* collisions, which conserve total electronic momentum. $\tau_{\mathbf{p}}$, on the other hand, like D_s, is sensitive to these collisions—indeed, they often provide the largest contribution to $\tau_{\mathbf{p}}^{-1}$.

Because the suppression of spin diffusion would at first sight seem detrimental to applications of spin transport, it is worth noting that quite the opposite may be the case. Indeed, if the the field of spintronics were ever to make the important grammatical shift from the subjunctive to the indicative, it might find sCd highly advantageous.

Spin Coulomb drag increases the distance that a spin packet can be dragged by an electric field, E, before it spreads due to diffusion. The length L_D that a packet of width w will drift before it broadens by a factor of two is $w^2 E\mu/D_s$. Thus

$$L_D = w^2 E \frac{\mu}{D_{c0}} \frac{\chi_s}{\chi_0} \left(1 + \frac{|\rho_{\uparrow\downarrow}|}{\rho} \right).$$

In the degenerate and nondegenerate regimes, respectively, the ratio μ/D_{c0} equals e/E_F or $e/k_B T$, and L_D is independent of the underlying scattering rates. In the degenerate regime, for example, in the absence of sCd we would have $L_D/w = eEw\chi_s/E_F\chi_0$; drifting a spin packet farther than

its own width would only be possible in a strong electric field, with the potential drop across the packet exceeding the Fermi energy. Introducing sCd slows the counterflow of spin $\uparrow$ and $\downarrow$ electrons without affecting their co-propagation, amplifying L_D by the factor $1+|\rho_{\uparrow\downarrow}(T)|/\rho$. Clean materials with strong e-e scattering will have the largest values of $\rho_{\uparrow\downarrow}/\rho$, and hence be the best media for propagation of spin information.

By a similar analysis, the distance a spin packet can drift before it decays is $L_{D'} = \mu E \tau_s$. DPK spin relaxation gives $\tau_s^{-1} \propto D_s$; that is, spin populations relax by diffusing. The sCd suppression of D_s, then, increases $L_{D'}$ by the same factor as L_D.

Bibliography

1. Datta, S. & Das, B. Electronic analog of the electro-optic modulator. *Applied Physics Letters* **56**, 665–7 (1990).

2. *Semiconductor Spintronics and Quantum Computation* (eds. Awschalom, D. D., Loss, D., and Samarth, N. Springer-Verlag, Berlin, 2002).

3. Bandyopadhyay, S. & Cahay, M. Reexamination of some spintronic field-effect device concepts. *Applied Physics Letters* **85**, 1433–5 (2004).

4. D'yakonov, M. I. Spintronics? In *Future Trends in Microelectronics: The Nano, the Giga, and the Ultra.* Eds. S. Luryi, J. Xu, and A. Zaslavsky, pp. 157-167. Wiley (2004). Cond-mat/0401369.

5. Ziman, J. M. *Electrons and phonons: the theory of transport phenomena in solids* (Oxford University Press, New York, 2001).

6. Weber, C. P., Gedik, N., Moore, J. E., Orenstein, J., Stephens, J. & Awschalom, D. D. Observation of spin Coulomb drag in a two-dimensional electron gas. *Nature* **437**, 1330–1333 (2005).

7. D'Amico, I. & Vignale, G. Spin diffusion in doped semiconductors: The role of Coulomb interactions. *Europhysics Letters* **55**, 566–572 (2001).

8. D'Amico, I. & Vignale, G. Spin Coulomb drag in the two-dimensional electron liquid. *Phys. Rev. B* **68**, 45307/1–7 (2003).

9. Si, Q. M. Probing spin-charge separation using spin transport. *Physica C* **341**, 1519–1522 (2000).

10. Cameron, A. R., Riblet, P. & Miller, A. Spin gratings and the measurement of electron drift mobility in multiple quantum well semiconductors. *Phys. Rev. Lett.* **76**, 4793–4796 (1996).

11. Meier, F. & Zakharchenya, B. *Optical Orientation* (North-Holland, Amsterdam, 1984).

12. Adachi, S., Muto, S. & Nelson, K. A. Spin diffusion and relaxation measurements by optical sampling four-wave-mixing technique. In *Technical Digest. Summaries of papers presented at the Quantum Electronics and Laser Science Conference*, p. 208 (Opt. Soc. America, 2001).

13. Kikkawa, J. M. & Awschalom, D. D. Lateral drag of spin coherence in gallium arsenide. *Nature* **397**, 139–141 (1999).

14. Flatté, M. E. & Byers, J. M. Spin diffusion in semiconductors. *Physical Review Letters* **84**, 4220–3 (2000).

15. D'yakonov, M. I. & Perel', V. I. Spin Orientation of Electrons Associated with Interband Absorption of Light in Semiconductors. *Sov. Phys. JETP* **33**, 1053–1059 (1971).

16. Gedik, N. & Orenstein, J. Absolute phase measurement in heterodyne detection of transient gratings. *Opt. Lett.* **29**, 2109–2111 (2004).

17. Vohringer, P. & Scherer, N. F. Transient Grating Optical Heterodyne Detected Impulsive Stimulated Raman-Scattering in Simple Liquids. *J. Phys. Chem.* **99**, 2684–2695 (1995).

18. Chang, Y. J., Cong, P. & Simon, J. D. Optical Heterodyne-Detection of Impulsive Stimulated Raman-Scattering in Liquids. *J. Phys. Chem.* **99**, 7857–7859 (1995).

19. Bastard, G. Electronic energy levels in semiconductor quantum wells and superlattices. *Superlattices & Microstructures* **1**, 265–73 (1985).

20. Bar-Ad, S. & Bar-Joseph, I. Exciton spin dynamics in GaAs heterostructures. *Phys. Rev. Lett.* **68**, 349–352 (1992).

21. Rammer, J. *Quantum transport theory* (Perseus Books, Reading, Mass., 1998).

22. Castellani, C., DiCastro, C., Kotliar, G., Lee, P. A. & Strinati, G. Thermal conductivity in disordered interacting-electron systems. *Phys. Rev. Lett.* **59**, 477–480 (1987).

23. Yarlagadda, S. & Giuliani, G. F. Spin susceptibility in a two-dimensional electron gas. *Phys. Rev. B* **40**, 5432–5440 (1989).

24. Kwon, Y., Ceperley, D. M. & Martin, R. M. Quantum Monte Carlo calculation of the Fermi-liquid parameters in the two-dimensional electron gas. *Phys. Rev. B* **50**, 16841694 (1994).

25. Rojo, A. G. Electron-drag effects in coupled electron systems. *Journal of Physics-Condensed Matter* **11**, R31–52 (1999).

26. Kato, Y. K., Myers, R. C., Gossard, A. C. & Awschalom, D. D. Observation of the spin Hall effect in semiconductors. *Science* **306**, 1910–1913 (2004).

27. Wunderlich, J., Kaestner, B., Sinova, J. & Jungwirth, T. Experimental observation of the spin-Hall effect in a two-dimensional spin-orbit coupled semiconductor system. *Phys. Rev. Lett.* **94**, 047204/1–4 (2005).

28. Flensberg, K., Jensen, T. S. & Mortensen, N. A. Diffusion equation and spin drag in spin-polarized transport. *Phys. Rev. B* **64**, 245308/1–7 (2001).

29. Burkov, A., Nunez, A. S. & MacDonald, A. Theory of spin-charge coupled transport in a two-dimensional electron gas with Rashba spin-orbit interactions (Version 2). *Cond-mat* 0311328 (2003).

30. Harris, J. J., Murray, R. & Foxon, C. T. Optical and electrical investigation of subband populations, mobilities and Fermi level pinning in δ-doped quantum wells. *Semiconductor Science & Technology* **8**, 31–8 (1993).

31. Terauchi, R., Ohno, Y., Adachi, T., Sato, A., Matsukura, F., Tackeuchi, A. & Ohno, H. Carrier mobility dependence of electron spin relaxation in GaAs quantum wells. *Japanese Journal of Applied Physics* **38**, 2549–51 (1999).

32. Fletcher, R., Feng, Y., Foxon, C. T. & Harris, J. J. Electron-phonon interaction in a very low mobility GaAs/Ga$_{1-x}$Al$_x$As δ-doped gated quantum well. *Physical Review B-Condensed Matter* **61**, 2028–33 (2000).

33. D'yakonov, M. I. & Perel, V. I. Spin Relaxation of Conduction Electrons in Noncentrosymmetric Semiconductors. *Sov. Phys. Solid State* **13**, 3023–3026 (1972).

34. Ohno, Y., Terauchi, R., Adachi, T., Matsukura, F. & Ohno, H. Spin relaxation in GaAs(110) quantum wells. *Physical Review Letters* **83**, 4196–9 (1999).

35. Miller, D. A. B., Chemla, D. S. & Schmitt-Rink, S. Relation between electroabsorption in bulk semiconductors and in quantum wells: the quantum-confined Franz-Keldysh effect. *Physical Review B-Condensed Matter* **33**, 6976–82 (1986).

36. Frankel, M. Y. & Carruthers, T. F. Transient Ellipsometric Surface Photoreflectance Applied to GaAs. *Applied Physics Letters* **64**, 1950–1952 (1994).

37. Fromer, N. A., Schuller, C., Lai, C. W., Chemla, D. S., Perakis, I. E., Driscoll, D. & Gossard, A. C. Coulomb correlations in a two-dimensional electron gas in large magnetic fields. *Physical Review B-Condensed Matter* **66**, 205314–1–13 (2002).

38. Erlingsson, S. I., Schliemann, J. & Loss, D. Spin susceptibilities, spin densities, and their connection to spin currents. *Physical Review B-Condensed Matter* **71**, 35319–1–6 (2005).

39. Lau, W. H., Olesberg, J. T. & Flatté, M. E. Electron-spin decoherence in bulk and quantum-well zinc-blende semiconductors. *Physical Review B-Condensed Matter* **64**, 161301/1–4 (2001).

40. Dyakonov, M. I. & Kachorovskii, V. Y. Spin Relaxation of Two-Dimensional Electrons in Noncentrosymmetric Semiconductors. *Soviet Physics Semiconductors-Ussr* **20**, 110–112 (1986).

41. Ohno, Y., Terauchi, R., Adachi, T., Matsukura, F. & Ohno, H. Electron spin relaxation beyond D'yakonov-Perel' interaction in GaAs/AlGaAs quantum wells. *Physica E: Low-dimensional Systems and Nanostructures* **6**, 817–820 (2000).

42. Adachi, T., Ohno, Y., Matsukura, F. & Ohno, H. Spin relaxation in n-modulation doped GaAs/AlGaAs (110) quantum wells. *Physica E: Low-dimensional Systems and Nanostructures* **10**, 36–9 (2001).

43. Fishman, G. & Lampel, G. Spin relaxation of photoelectrons in p-type gallium arsenide. *Physical Review B (Solid State)* **16**, 820–31 (1977).

44. Tackeuchi, A., Nishikawa, Y. & Wada, O. Room-temperature electron spin dynamics in GaAs/AlGaAs quantum wells. *Applied Physics Letters* **68**, 797–9 (1996).

45. Britton, R. S., Grevatt, T., Malinowski, A., Harley, R. T., Perozzo, P., Cameron, A. R. & Miller, A. Room temperature spin relaxation in GaAs/AlGaAs multiple quantum wells. *Applied Physics Letters* **73**, 2140–2142 (1998).

46. Malinowski, A., Britton, R. S., Grevatt, T., Harley, R. T., Ritchie, D. A. & Simmons, M. Y. Spin relaxation in GaAs/Al$_x$Ga$_{1-x}$As quantum wells. *Physical Review B-Condensed Matter* **62**, 13034–9 (2000).

47. Bournel, A., Dollfus, P., Cassan, E. & Hesto, P. Monte Carlo study of spin relaxation in AlGaAs/GaAs quantum wells. *Applied Physics Letters* **77**, 2346–8 (2000).

48. Glazov, M. M. & Ivchenko, E. L. Precession spin relaxation mechanism caused by frequent electron-electron collisions. *Jetp Letters* **75**, 403–405 (2002).

49. Brand, M. A. *et al.* Precession and motional slowing of spin evolution in a high mobility two-dimensional electron gas. *Physical Review Letters* **89**, 236601–1–4 (2002).

50. Dzhioev, R. I. *et al.* Suppression of Dyakonov-Perel spin relaxation in high-mobility n-GaAs. *Physical Review Letters* **93** (2004).

51. Zutic, I., Fabian, J. & Das Sarma, S. Spintronics: Fundamentals and applications. *Reviews of Modern Physics* **76**, 323–410 (2004).

Appendix A

Experimental details

A.1 Preparing samples

Jason Stephens grows our GaAs quantum well samples by molecular beam epitaxy on top of a GaAs wafer. The wafer's crystal directions and specifications appear in Fig. A.1. When we get the samples, they are in the form of a piece cut from the center of such a wafer, roughly 1.5 cm on a side. Each sample we measure is yet a smaller piece cut from one of these pieces, and prepared thinned for optical transmission as follows.

The piece is cleaved off by scoring in a straight line with a diamond-tipped scribe, then using a ruler to deliver a sharp blow along that line. The piece is then epoxied face-down (quantum-well-down) onto a sapphire substrate. The epoxy is Devcon no. 14260 (because that's what Jason uses; it's available from McMaster-Carr). If the epoxy is not mixed to the right ratio it takes a long time to set, and perhaps never completely sets—I've seen samples begin to slide off of the sapphire substrate when heated on a hot-plate. Normally the epoxy cures overnight, with a weight pressing the GaAs down to keep it flush to the sapphire.

The sapphire is from Almaz Optics, and is c-cut so that it is not birefringent (at least, for light at normal incidence). It is 1.14 mm thick. (Earlier samples were glued onto sapphire that Jason provided, which was also c-cut but 0.5 mm thick.) I opted for the thicker substrates because in the pump-probe experiment reflections off of the substrate introduce a glitch in the time-trace. The thicker substrate puts these "bad points" at a later time, where they are generally less troublesome. The thick substrate is, however, hard to cleave: first one must score it on both sides and the edges with a diamond-scribe reserved for this purpose (presumably by now very blunt), then clamp the piece along the scored line, then strike it with a hammer.

Once the GaAs is epoxied to the substrate, the wafer must be removed so that the resulting
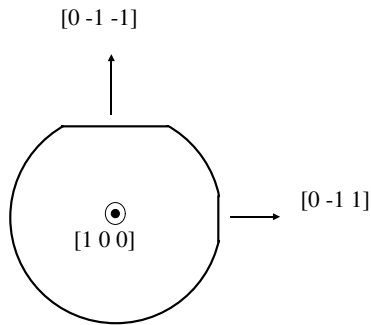
Figure A.1. Crystal axis directions for the wafers on which Jason Stephens grows our quantum well samples. Pieces cut from these wafers are marked with an "X" indicating the side on which the quantum well is *not* grown, and a line parallel to the direction of the longer of the two flattened edges. The wafers are from Wafer Technology Ltd., UK, with specifications: cut (100) ±0.1°; undoped, semi-insulating; DS polished; 500±25μm thick.

sample (quantum well plus sapphire) is sufficiently transparent to light at 800 nm. Much of this process I learned from Jason during a visit of 8 July 2004.

The first step is mechanical polishing: the sample is waxed (sapph down) onto a polishing-puck, then polished by hand to remove the first 400 μm or so of the wafer. For wax one may use either Apiezon-W or Aremco Crystal Bond. I prefer the Apiezon because it has a lower melting temperature, so one needn't get the sample so hot when waxing (or un-waxing) it. (It's heated by placing the polishing-puck on a hot plate.) However, the Aremco is supposed to be removable with acetone (perhaps hot acetone), while the Apiezon requires chloroform. Chloroform will attack the epoxy, so one must apply it carefully, with a dropper.

The hand-polishing is done on pads with 9 μm grit attached to the surface (available from Buehler, no. 69-3271). The thickness of the sample plus puck is measured with calipers beforehand and frequently during the polishing to ensure that too much GaAs is not removed. Removing 400 μm typically takes about 20 minutes and uses up one or two pads.

The sample is then de-waxed from the puck (heated and removed), and the wax removed (see above). The remainder of the wafer is then chemically etched away. (The lowest layer grown by MBE is a "stop-etch" layer: 500 nm of $Al_{0.3}Ga_{0.7}As$, which etches much more slowly than GaAs.) The etchant is a mixture of 200 ml 30% H_2O_2 with 6 ml 20% NH_4OH. By blowing N_2 through a glass contraption, the etchant is sprayed onto the sample as a a stream of droplets (the sample is held vertically so that the etchant runs off). One can tell when the stop-etch layer is reached because the sample's surface will go from a mat to a gloss finish (since the stop-etch layer is atomically flat). This process is finicky (about a 25% success rate), and should be watched carefully to avoid

etching away the entire sample. The etching can take anywhere from minutes to hours, depending (in part, I believe) on the freshness of the chemicals. The most common way it fails is for the sample to begin to grow shiny from the edge first; usually samples that etch successfully reach the stop-etch layer first in the middle.

The sample is then mounted on a Cu block that can be attached to the cryostat's cold-finger (see Section A.2). Since it is measured in transmission, it is placed over a hole (which is drilled out to the size of the sample—but no larger, to keep the thermal contact good) and on top of a piece of indium foil. Another piece of In foil and a Cu plate (with holes in them, of course) are placed on top of the sample, and screwed down as tightly as is safe without cracking the sapphire.

A.2   Cryostats

The angle between the two pump beams incident on the sample determines the grating's q. In order to measure at high q, one needs a cryostat that allows large incident angles; so the cryostat's front and back windows ought to be large and close together. For all of the data presented in this work, the cryostat was an Oxford Microstat. We have now replaced this with a Janis ST-300MS, which appears to be nearly equivalent. Both are cold-finger cryostats, in which the sample is mounted on a copper block attached to the end of the cryostat's cold finger. (In the Oxford, the temperature sensor was mounted on this copper block; in the Janis, it is mounted on the cold finger.) These copper blocks are interchangeable, so once a sample is mounted on one it need never be de-mounted. Typically the sample's name is scratched onto the surface of the block.

To improve the cryostat's stability, when the LHe transfer line is connected, the LHe dewar is belted to the optical table. The cryostat is pumped before an experiment, but not during. On warming from low temperature, the Oxford would outgas, making the vacuum "soft": condensation would appear on the windows. To prevent condensation, dry N_2 gas was blown onto both windows during warming.

The cryostat works best if one pumps on the He outlet (not with a vacuum pump). The flow can then be regulated with a gauge/valve on the He outlet. The Janis will reach 7 K with a flow of 30 SCFH; at maximum flow, it reaches 4.5 K.

A.3   Phase masks

A phase mask works essentially as a diffraction grating in transmission, but puts a larger fraction of the incident light into the ± 1 diffracted orders. Ours were made for us *circa* August 2002 by Digital Optics Co. They consist of arrays of ten phase masks on a single fused silica substrate (we have several identical arrays of this type). The phase masks are optimized for light of wavelength

100	120	140	160	200
1.26	1.51	1.76	2.01	2.51
250	300	360	420	500
3.14	3.77	4.53	5.28	6.29

Figure A.2. Layout of phase mask array. The top number shown is the number of grooves per mm, n; the bottom number is the wavevector, q, of the grating formed on the sample by the interference of the ± 1 diffracted orders. The q shown here is in units of 10^4 cm^{-1}. Notice that $q = 4\pi n$. A picture of the phase mask array appears in Fig. A.3. The n of each phase mask is printed next to it on the fused silica substrate in very small numerals.

$\lambda = 800$ nm. They vary in their number of "grooves" per mm, and are laid out as shown in Fig. A.2. A picture of the phase mask array appears in Fig. A.3.

Once the phase mask has split the pump and probe beams into the ± 1 orders, the resulting four beams must be focused back together on the sample. We accomplish this with a large, spherical mirror with radius of curvature 12.204 inches (made for us by A.M.F. Optics, and gold-coated by International μicro Photonix). For transient gratings with $q > 3.14 \times 10^4$ cm^{-1}, the ± 1 orders do not fit on this mirror. However, we have bought larger mirrors (with the same radius of curvature) that will allow us to measure up to the highest q available on the phase mask array.

The optics are aligned such that both the phase mask and the sample are at the "center" of the mirror's sphere (with a folding-mirror in between), so that the angle θ by which each ± 1 order is diffracted is the same as the angle θ at which the beam is incident on the sample, measured from the normal. For n grooves per mm, interference of the ± 1 orders on the sample results in a grating with wavelength $\Lambda = 1/2n$ (if it were the 0 & +1 or 0 & -1 orders interfering, the factor of 2 would not appear). Thus $q = 4\pi n$.

The limit on how *low* of a q we can measure is set by how low-n of a diffraction grating (in transmission) we can buy. We bought gratings from Edmund Scientific, and glued them together into an array, laid out as shown in Fig. A.4. To minimize re-alignment when switching from the phase mask array to the Edmund grating array, the +1 order should be diffracted downwards.
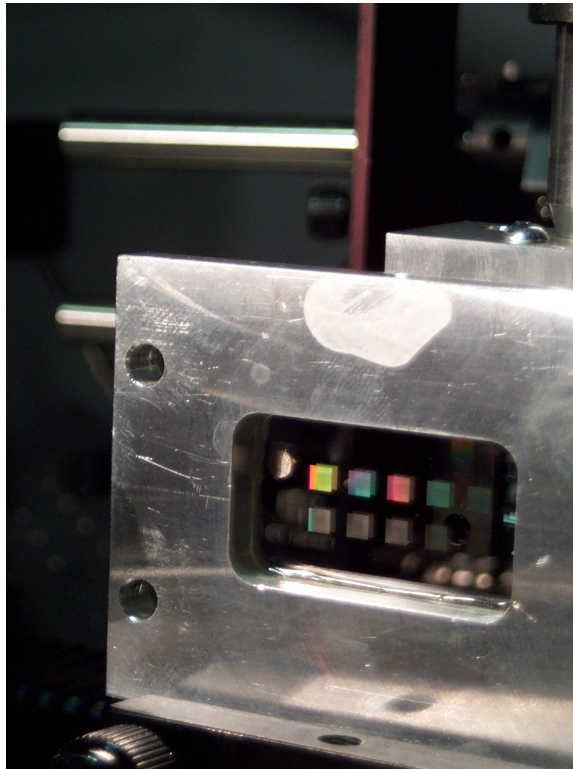
Figure A.3. The phase-mask array, in an aluminum holder.

70	80	92	110
0.44	0.50	0.58	0.69
n/a	1.01	1.16	1.38

Figure A.4. Layout of the array of Edmund gratings. The top number shown is the number of grooves per mm, n; the middle number is the wavevector, q, of the grating formed on the sample by the interference of the 0 & +1 diffracted orders; the bottom, by the ±1 orders. (q is shown in units of 10^4 cm^{-1}.) The $n = 70$ grating puts most of the incident beam's power into the 0 and +1 orders, and little into the -1, so no q is listed for ±1. The other gratings put roughly equal amounts of light into -1, 0, and +1. Part numbers are recorded in the lab book entry for 23 February 2005.

45